

# *Geomechanical modeling of stresses adjacent to salt bodies: Part 1—Uncoupled models*

**Gang Luo, Maria A. Nikolinakou, Peter B. Flemings, and Michael R. Hudec**

## **ABSTRACT**

We compare four approaches to geomechanical modeling of stresses adjacent to salt bodies. These approaches are distinguished by their use of elastic or elastoplastic constitutive laws for sediments surrounding the salt, as well as their treatment of fluid pressures in modeling. We simulate total stress in an elastic medium and then subtract an assumed pore pressure after calculations are complete; simulate effective stress in an elastic medium and use assumed pore pressure during calculations; simulate total stress in an elastoplastic medium, either ignoring pore pressure or approximating its effects by decreasing the internal friction angle; and simulate effective stress in an elastoplastic medium and use assumed pore pressure during calculations. To evaluate these approaches, we compare stresses generated by viscoelastic stress relaxation of a salt sphere. In all cases, relaxation causes the salt sphere to shorten vertically and expand laterally, producing extensional strains above and below the sphere and shortening against the sphere flanks. Deviatoric stresses are highest when sediments are assumed to be elastic, whereas plastic yielding in elastoplastic models places an upper limit on deviatoric stresses that the rocks can support, so stress perturbations are smaller. These comparisons provide insights into stresses around salt bodies and give geoscientists a basis for evaluating and comparing stress predictions.

## **INTRODUCTION**

Drilling into and through salt systems has proven challenging, dangerous, and expensive (e.g., Sweatman et al., 1999; Whitson and McFadyen, 2001; Rohleder et al., 2003; Willson

## **AUTHORS**

**GANG LUO** ~ Bureau of Economic Geology, Jackson School of Geosciences, University of Texas at Austin, Austin, Texas 78713; [gangluo66@gmail.com](mailto:gangluo66@gmail.com)

Gang Luo received his Ph.D. in computational geodynamics from the University of Missouri at Columbia in 2009, and then he joined the Bureau of Economic Geology. His current research interests include wellbore stability analysis, poromechanical modeling in stress and pore pressure of sedimentary basins, numerical modeling in salt tectonics, and finite-element modeling in geodynamic processes of crust and lithosphere.

**MARIA A. NIKOLINAKOU** ~ Bureau of Economic Geology, Jackson School of Geosciences, University of Texas at Austin, Austin, Texas 78713; [mariakat@mail.utexas.edu](mailto:mariakat@mail.utexas.edu)

Maria Nikolinakou received her Sc.D. degree in theoretical soil mechanics from Massachusetts Institute of Technology in 2008. She then worked for Shell Exploration and Production in reservoir geomechanics. She joined the Bureau of Economic Geology in 2009, where she is now a research associate. Her current research includes poromechanical modeling of basin sediments, geomechanical pore-pressure prediction, and numerical modeling in salt tectonics.

**PETER B. FLEMINGS** ~ Bureau of Economic Geology, Jackson School of Geosciences, University of Texas at Austin, Austin, Texas 78713; [pflemings@jsg.utexas.edu](mailto:pflemings@jsg.utexas.edu)

Peter B. Flemings is the Jackson Professor of Geosystems at the University of Texas at Austin. Previously, he taught in the Department of Geosciences at Penn State. He received his B.A. degree from Dartmouth College and his M.S. and Ph.D. in geology from Cornell University. His research focuses on the study of fluid flow, pressure, and stress in sedimentary basins.

**MICHAEL R. HUDEC** ~ Bureau of Economic Geology, Jackson School of Geosciences, University of Texas at Austin, Austin, Texas 78713; [michael.hudec@beg.utexas.edu](mailto:michael.hudec@beg.utexas.edu)

Mike Hudec received his Ph.D. from the University of Wyoming in 1990. After working for Exxon Production Research and Baylor University, he joined the Bureau of Economic Geology

---

Copyright ©2012. The American Association of Petroleum Geologists. All rights reserved.

Manuscript received September 1, 2010; provisional acceptance January 5, 2011; revised manuscript received March 22, 2011; final acceptance April 11, 2011.

DOI:10.1306/0411110144

in 2000, where he is codirector of the Applied Geodynamics Laboratory. His current research interests include palinspastic restoration of salt structures and early history of the Gulf of Mexico salt basin.

## ACKNOWLEDGEMENTS

This work was supported by the Applied Geodynamics Laboratory Industrial Associates Program and UT Geofluids Industrial Associates Program. Members of the Applied Geodynamics Laboratory consortium include Anadarko, BHP Billiton, BP, CGCVeritas, Chevron, Cobalt, ConocoPhillips, Ecopetrol, ENI, ExxonMobil, Fugro, Global Geophysical, Hess, IMP, INEXS, ION Geophysical, Maersk, Marathon, Mariner, McMoRan, Murphy, Nexen, Noble, Pemex, Petrobras, PGS, Repsol-YPF, Samson, Saudi Aramco, Shell, Statoil, TGS-NOPEC, Total, WesternGeco, and Woodside. Members of the UT Geofluids consortium include Anadarko, BHP Billiton, BP, Chevron, ConocoPhillips, Devon, ExxonMobil, Hess, Schlumberger, Shell, Statoil, and Total. We thank AAPG editor Stephen E. Laubach and reviewers Tricia Allwardt, Markus Albertz, and Jon Olson for review comments and constructive suggestions. We benefited from discussions with Glen Bowers and Mark Zoback. Lana Dieterich edited the manuscript. Publication was authorized by the Director, Bureau of Economic Geology, Jackson School of Geosciences, The University of Texas at Austin. The AAPG Editor thanks the following reviewers for their work on this paper: Markus Albertz and Tricia F. Allwardt.

and Fredrich, 2005). One reason is that stresses and fluid pressures adjacent to salt may be highly perturbed relative to their regional values (e.g., Bradley, 1978; Whitson and McFadyen, 2001; Rohleder et al., 2003; Dusseault et al., 2004). Predicting the magnitude of these anomalies is also challenging (e.g., Rohleder et al., 2003; Willson et al., 2003; Willson and Fredrich, 2005).

An obvious solution to this problem is to use geomechanical models to simulate stresses and fluid pressures around salt bodies (e.g., Fredrich et al., 2003, 2007; Kouprianchik et al., 2005; Mackay et al., 2008). However, geomechanical modeling has yet to produce a clear consensus on what stress fields adjacent to salt should look like, the magnitude of predicted stress effects, or even the proper techniques to use in the modeling. Two key areas of disagreement in modeling are (1) what constitutive laws are appropriate to describe sediments surrounding the salt and (2) how fluid pressures are simulated. These choices, in turn, depend on the scale of the structures being modeled and the time frames being simulated.

At basin scales and geologic time frames, viscous, viscoplastic, frictional-plastic, and elastoplastic constitutive models are used to describe sediments during the evolution of salt systems. These models have explored driving forces in salt basins (e.g., Daudré and Cloetingh, 1994; Gil and Jurado, 1998), developments of salt structures and associated faults and folds (e.g., Podladchikov et al., 1993; Poliakov et al., 1993b, 1996; Schultz-Ela, 2003; Dirkzwager and Dooley, 2008), and development of sedimentary basins (e.g., Gemmer et al., 2004, 2005; Ings et al., 2004). However, when modeling effects of single salt structures over short time scales (e.g., the topic of this article), most workers have used elastic or elastoplastic constitutive laws to model sediments adjacent to salt (Table 1).

In some of these models, fluid pressures are ignored (e.g., Fredrich et al., 2003, 2007; Sanz and Dasari, 2010) or indirectly incorporated as a reduction in the internal friction angle of sediments (e.g., Gemmer et al., 2004, 2005; Ings et al., 2004). We refer to these models as uncoupled models because they do not consider fluid flow or interactions between the fluid and solid matrix. In a companion article (Nikolinakou et al., 2012), we present our preliminary attempts at explicitly modeling fluid flow around salt in a fully coupled model.

To the nonspecialist, this range of approaches is confusing. How do modeling assumptions affect results? How can results published by separate authors be compared? Which approaches most closely approximate subsurface geology? In this article, we describe each of the published modeling techniques, illustrate how model results differ from one another, and discuss

**Table 1.** Summary of Uncoupled Model Types and Model Cases Described in This Article

Model Type	Elastic Sediments	Elastoplastic Sediments
Solve governing equations in total-stress system	Case 1: Ignore pore pressure and simulate total stress (e.g., Fredrich et al., 2003, 2007; Kouprianchik et al., 2005; Mackay et al., 2008; Sanz and Dasari, 2010). Subtract distribution of pore pressure (such as hydrostatic pore pressure) from modeled total stress field to calculate effective-stress field.	Case 3A: Ignore pore pressure and simulate total stress (e.g., Schultz-Ela et al., 1993; Schultz-Ela and Jackson, 1996; Schultz-Ela and Walsh, 2002; Sanz and Dasari, 2010). Case 3B: Simulate total stress and consider effects of hydrostatic pore pressure by decreasing internal friction angle in modeling (e.g., Schultz-Ela, 2003). Note that pore pressure is not truly included in the models.
Solve governing equations in effective-stress system	Case 2: Substitute distribution of pore pressure (such as hydrostatic pore pressure) into governing equations and simulate effective stress. Total stress field is calculated by summing of effective-stress field and pore pressure. Resulting total and effective stresses are the same as those predicted by case 1.	Case 4: Substitute distribution of pore pressure (such as hydrostatic pore pressure) into governing equations and simulate effective stress (e.g., Poliakov et al., 1993a, 1996; Dirkzwager and Dooley, 2008).

the advantages and limitations of each approach. Furthermore, our discussion of deformation and stress patterns that accompany relaxation of a salt sphere should provide some physical insight into why stresses are perturbed around salt and why different stress states occur around different parts of a salt body.

## PUBLISHED MODELING APPROACHES

We subdivide published models into four types, according to (1) whether they assume elastic or elastoplastic constitutive laws for sediments and (2) how or whether they simulate the effects of fluid pressure (Table 1). We define each of these approaches and discuss how they have been used to study deformation and stresses around salt.

Stress applied to the whole system, including the solid matrix and fluid, is called total stress. In a system that includes pore fluid, some of the total stress is supported by pore fluid, reducing the amount of stress felt by the solid matrix. The fraction of total stress supported by the solid matrix is called effective stress (Terzaghi, 1925). The relation between total stress,  $\sigma_{ij}$ , effective stress,  $\sigma'_{ij}$ , and pore pressure,  $u$ , can be expressed as  $\sigma'_{ij} = \sigma_{ij} - \delta_{ij}u$  ( $i, j = 1, 2, 3$ )

(Terzaghi, 1925; see definitions of variables in Table 2). Effective stress is important because it is used to compute plastic yielding of sediments in elastoplastic models (e.g., Wood, 1990), and thus, control wellbore stability analysis and drilling trajectory (e.g., McLean and Addis, 1990; Zoback, 2007).

Elasticity does not have yield. However, plasticity has a yield criterion, constraining the magnitude of deviatoric stresses (e.g., Wood, 1990; Dunne and Petrinic, 2005; Jaeger et al., 2007). Deviatoric stress is the part of the stress tensor that causes distortion (e.g., Jaeger et al., 2007, p. 40). Both elastic and elastoplastic constitutive laws have been used in models of salt systems (e.g., Poliakov et al., 1996; Fredrich et al., 2003; Dirkzwager and Dooley, 2008).

### Case 1: Elastic Models, Calculated in Total Stress

An elastic model assumes that sediments are elastic solids (no pores, and hence, no pore pressure). This approach may be the one most commonly used in finite-element modeling of stresses around salt structures. Fredrich et al. (2003, 2007) and Mackay et al. (2008) used the finite-element method to simulate stress relaxation within salt and stress

**Table 2.** Nomenclature

Variable	Description	Unit	Dimensions
$E$	Young's modulus	Pa	$ML^{-1}T^{-2}$
$\nu$	Poisson's ratio	—	—
$g$	Gravitational acceleration	$m/s^2$	$LT^{-2}$
$\rho$	Bulk density	$kg/m^3$	$ML^{-3}$
$\rho_{\text{sed}}$	Bulk density of sediments	$kg/m^3$	$ML^{-3}$
$\rho_{\text{salt}}$	Bulk density of salt bodies	$kg/m^3$	$ML^{-3}$
$\rho_w$	Bulk density of water	$kg/m^3$	$ML^{-3}$
$\eta$	Viscosity of salt bodies	Pa s	$ML^{-1}T^{-1}$
$\phi$	Internal friction angle of sediments	Degree	Degree
$\phi_{\text{eff}}$	"Effective" internal friction angle of sediments	Degree	Degree
$C$	Cohesion of sediments	Pa	$ML^{-1}T^{-2}$
$C_{\text{eff}}$	"Effective" cohesion of sediments	Pa	$ML^{-1}T^{-2}$
$\lambda$	Ratio of pore pressure and solid pressure	—	—
$\lambda_{\text{HR}}$	Hubbert-Rubey pore pressure ratio	—	—
$K_0^T$	Ratio of minimum and maximum principal total stresses	—	—
$K_0$	Ratio of minimum and maximum principal effective stresses	—	—
$\delta_{ij}$	Kronecker delta function, when $i = j$ , $\delta_{ij} = 1$ ; when $i \neq j$ , $\delta_{ij} = 0$	—	—
$u$	Pore pressure	Pa	$ML^{-1}T^{-2}$
$P$	Solid pressure	Pa	$ML^{-1}T^{-2}$
$\sigma$	Total stress	Pa	$ML^{-1}T^{-2}$
$\sigma'$	Effective stress	Pa	$ML^{-1}T^{-2}$
$\Delta\sigma$	Perturbation of stress	Pa	$ML^{-1}T^{-2}$
$\sigma_{ij}$	Stress components of total stress tensor	Pa	$ML^{-1}T^{-2}$
$\sigma_{rr}$	Radial total stress	Pa	$ML^{-1}T^{-2}$
$\sigma_{zz} = \sigma_v$	Vertical total stress	Pa	$ML^{-1}T^{-2}$
$\sigma_{\theta\theta}$	Out-of-plane (or hoop) total stress	Pa	$ML^{-1}T^{-2}$
$\sigma_{rz}, \sigma_{r\theta}, \sigma_{z\theta}$	Three shear stress components of total stress tensor	Pa	$ML^{-1}T^{-2}$
$\sigma_H$	Maximum horizontal principal total stress	Pa	$ML^{-1}T^{-2}$
$\sigma_h$	Minimum horizontal principal total stress	Pa	$ML^{-1}T^{-2}$
$\sigma_1$	Maximum principal total stress	Pa	$ML^{-1}T^{-2}$
$\sigma_2$	Intermediate principal total stress	Pa	$ML^{-1}T^{-2}$
$\sigma_3$	Minimum principal total stress	Pa	$ML^{-1}T^{-2}$
$\sigma_{VM}$	Von Mises stress	Pa	$ML^{-1}T^{-2}$
$\varepsilon_1^{pl}$	Maximum principal strain of plastic strain tensor	—	—
$\varepsilon_2^{pl}$	Intermediate principal strain of plastic strain tensor	—	—
$\varepsilon_3^{pl}$	Minimum principal strain of plastic strain tensor	—	—
$\varepsilon_{\text{Plastic}}$	Plastic strain magnitude	—	—

perturbations around salt bodies. They used power-law nonlinear viscoelastic salt bodies and investigated different salt geometries, including a sphere, an idealized horizontal sheet, an idealized vertical dome, a vertical dome with an overlying tongue, and a true complex salt-diapir geometry from the Gulf of Mexico. Kouprianchik et al. (2005) used

the finite-difference method to model salt-stress relaxation and stress perturbations around salt of the Munta diapir in the Officer Basin, south Australia. They investigated both power-law nonlinear and Maxwell linear viscoelastic salt bodies and found no difference in final static stresses predicted by the two salt constitutive laws. These

models considered processes related to viscoelastic stress relaxation of salt, but did not consider geodynamic processes of salt motion.

All these models are calculated using total stress (see equation 1 in Appendix). As an optional final step, an assumed pore-pressure distribution may be subtracted from the final stresses to produce a result in effective stress (e.g., Fredrich et al., 2003). However, in this case, pore pressure is assumed, not calculated. Furthermore, the presence of fluids plays no role in computation. The only purpose of adding fluid pressure at the end of modeling is to permit comparison with other results calculated using effective stress (see cases 2 and 4).

### **Case 2: Elastic Models, Calculated in Effective Stress**

This approach, as in case 1, assumes an elastic constitutive law for sediments. However, an assumed pore-pressure distribution is included in the governing equations (see equation 2 in Appendix), and then all computations are performed using effective stress. For solution of elastic problems, cases 1 and 2 provide equivalent results. Pore pressure is included in the modeling, and the problem is solved in effective stress, but no fluid flow, fluid dissipation, or interaction between fluid and the solid matrix exists in this case.

### **Case 3: Elastoplastic Models, Calculated in Total Stress**

Plasticity has also been used to simulate stress-strain behavior of sediments around salt. Plasticity introduces limits on deviatoric stresses and simulates irrecoverable or permanent deformation (e.g., Wood, 1990; Roylance, 1996), making elastoplastic models more realistic than elastic models (e.g., Bowers, 2007).

In some instances, elastoplastic models ignore the effects of pore pressure, solving the governing equations in total stress (case 3A). Schultz-Ela et al. (1993) used linear viscoelastic salt and elastoplastic sediments with strain softening in finite-element modeling to investigate initiation and development of faults near a salt diapir. The same approach was

applied by Schultz-Ela and Jackson (1996) to simulate linkage of fault patterns above and below the salt in extensional regimes. Similarly, Schultz-Ela and Walsh (2002) applied this approach in exploring the development of faults above a salt layer and interaction between extending overburden and the underlying salt layer in finite-element models. These models have somewhat limited use because of the importance of effective stress in plastic yield.

In other models, the effects of pore pressure are commonly approximated and simulated by assuming a low internal friction angle (case 3B). This angle is commonly called the “effective” internal friction angle in many articles (e.g., Ings et al., 2004; Gemmer et al., 2005). Using this approach, Schultz-Ela (2003) incorporated linear viscoelastic salt and elastoplastic sediments with strain softening to simulate initiation, growth, and evolution of drag folds around a salt-diapir system by finite-element modeling. This approach has also been applied widely to simulate the effects of pore pressure on viscoplastic models for geologic evolution of a sedimentary basin in salt tectonic systems (e.g., Ings et al., 2004; Gemmer et al., 2005). Note that varying the internal friction angle is only a proxy for pore pressure. Because the model contains neither pore pressure nor pore space, no computations of fluid flow or fluid pressure exist. Also, because the internal friction angle is everywhere the same and does not change during the experiment, it allows for no change of pore pressure during deformation (see Appendix).

### **Case 4: Elastoplastic Models, Calculated in Effective Stress**

Other elastoplastic models incorporate pore pressure by calculating results using effective stress. They do so by assuming a pore-pressure field (commonly hydrostatic) and substituting it into the governing equations (see equation 2 in Appendix), and then models are calculated in effective stress. The models are uncoupled because pore pressure is assumed and not recalculated during the simulation. Dirkzwager and Dooley (2008) assumed hydrostatic pore pressure and used elastoplastic (Drucker-Prager plasticity) sediments to simulate stresses and deformation of a salt-based gravity-driven fold and thrust

belt. Poliakov et al. (1993a) assumed hydrostatic pore pressure and applied an elastoplastic (Mohr-Coulomb plasticity) constitutive law to sediments to explore the initiation of salt diapirs. Poliakov et al. (1996) assumed hydrostatic pore pressure and used viscoelastoplastic sediments (Mohr-Coulomb plasticity) to simulate brittle deformation within the overburden above salt diapirs.

In this study, we compare these uncoupled modeling approaches using two-dimensional (2-D) axisymmetric finite-element models to explore deformation and stresses around a spherical salt body caused by viscoelastic stress relaxation of the salt. We compare these approaches by describing their differences and similarities in model results and pointing out model limitations. These results provide a basis for interpreting and comparing published finite-element models involving salt and offer insight into stress and deformation patterns around salt structures.

## MODEL SETUP

We study salt bodies encased in their surrounding sediments and represent the three-dimensional (3-D) geometry with an axisymmetric model (Figure 1). In all simulations, the radius of the model domain is 20 km (12.4 mi). No normal displacements occur along the outer boundary ( $r = 20$  km [12.4 mi],

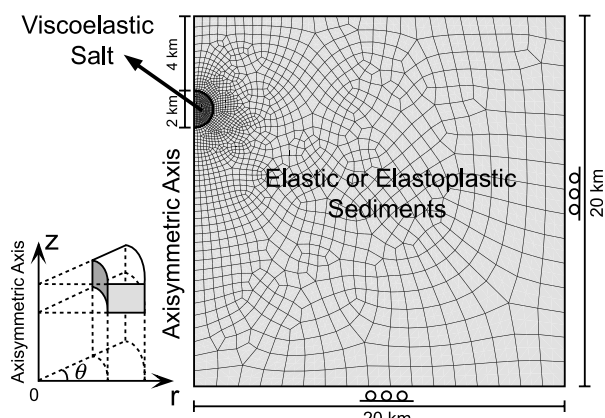


**Figure 1.** The finite-element mesh for the salt sphere and model boundary conditions. Dark-gray and light-gray elements show the salt structure and sediments, respectively.

**Table 3.** Material Parameters in Modeling

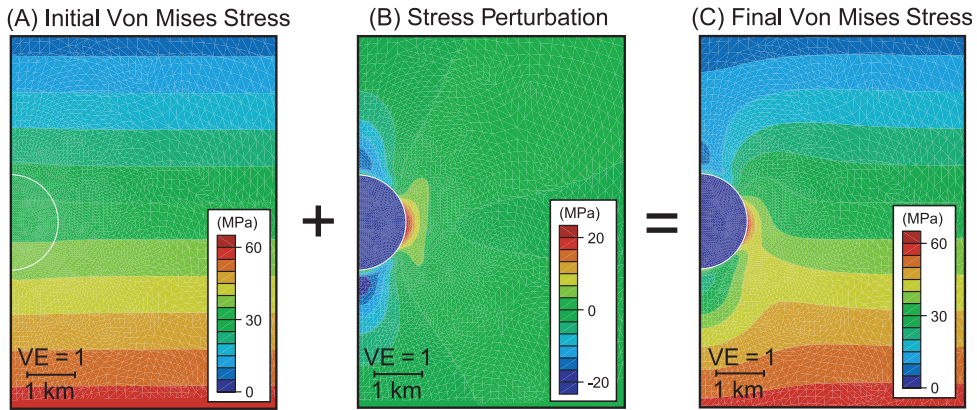
Material Parameters	Salt	Sediments
Density $\rho$ (kg/m <sup>3</sup> )	2076.5	2220
Young's modulus $E$ (Pa)	$3.1 \times 10^{10}$	$6 \times 10^9$
Poisson's ratio $\nu$	0.25	0.225
Viscosity $\eta$ (Pa s)	$10^{18}$	—
Internal friction angle $\phi$ (°)	—	30
Cohesion $C$ (MPa)	—	0.03
"Effective" internal friction angle $\phi_{\text{eff}}$ (°)	—	15.95 in case 3B
"Effective" cohesion $C_{\text{eff}}$ (MPa)	—	0.027 in case 3B
Water density $\rho_w$ (kg/m <sup>3</sup> )	1000	—
Gravitational acceleration $g$ (m/s <sup>2</sup> )	9.81	—

Figure 1) and the base ( $z = 0$  km, Figure 1). The top boundary ( $z = 20$  km [12.4 mi], Figure 1) is free. Along the central axis ( $r = 0$  km, Figure 1), axisymmetric boundary conditions are applied.

Salt is modeled as a linear viscoelastic Maxwell body (equations 3–5 in Appendix). Because salt bodies are assumed to be impermeable, they have no pore pressure. Sediments are assumed to be of either an elastic (cases 1 and 2) or a perfectly elastoplastic (cases 3 and 4) material using either the Drucker-Prager or the Mohr-Coulomb plastic yield criteria (equations 6–13 in Appendix). Material parameters are shown in Table 3. Pore pressure in sediments is assumed to be hydrostatic.

We use the commercial finite-element analysis software, Abaqus, to simulate processes of viscoelastic salt-stress relaxation in two steps. First, we solve for an equilibrated initial stress field for the model domain using material constitutive laws, material parameters (Table 3), an assumed horizontal to vertical stress ratio, and boundary conditions. Second, on the basis of the initial stress field, we simulate salt viscoelastic stress relaxation until von Mises stress ( $\sigma_{\text{VM}}$ ) within salt bodies decays to less than 0.1 MPa (<14.5 psi). The von Mises stress is a measure of deviatoric stresses in three dimensions:

$$\begin{aligned} \sigma_{\text{VM}} &= \sqrt{\frac{1}{2}[(\sigma_1 - \sigma_2)^2 + (\sigma_1 - \sigma_3)^2 + (\sigma_2 - \sigma_3)^2]} \\ &= \sqrt{\frac{1}{2}[(\sigma'_1 - \sigma'_2)^2 + (\sigma'_1 - \sigma'_3)^2 + (\sigma'_2 - \sigma'_3)^2]} \end{aligned} \quad (1)$$



**Figure 2.** The final stress field is the sum of the initial stress field and stress perturbations caused by salt viscoelastic stress relaxation: (A) initial von Mises stress field, (B) perturbations of von Mises stress, and (C) final static von Mises stress field. These results are predicted by the elastic model in case 1. The white semi-circle is the interface between salt and sediments. The case number is shown in Table 1 and material parameters are shown in Table 3. VE = vertical exaggeration.

where  $\sigma_1$ ,  $\sigma_2$ ,  $\sigma_3$ , and  $\sigma'_1$ ,  $\sigma'_2$ ,  $\sigma'_3$  are principal total and effective stresses, respectively. During the second modeling step, viscoelastic salt bodies cannot sustain initial deviatoric stresses, which have developed within the salt during the static initialization process (the first modeling step), so deviatoric stresses or von Mises stress within the salt decay over time. As a response to salt-stress relaxation and force equilibrium, stresses in the surrounding sediments are perturbed.

In both salt bodies and sediments, initial total horizontal stresses ( $\sigma_H = \sigma_{rr} = \sigma_{\theta\theta}$ ) are assumed proportional to the total vertical stress ( $\sigma_V$ ):

$$K_0^T = \frac{\sigma_H}{\sigma_V} \quad (2)$$

where  $K_0^T$ , total-stress ratio, is assumed to be equal to 0.7. In the Appendix, we show that for hydrostatic conditions with  $K_0^T$  equal to 0.7, the equivalent effective-stress ratio,  $K_0$ , equals 0.454 ( $K_0 = \sigma'_H/\sigma'_V$ ).

We incorporate hydrostatic pressure in one of two ways. First, the force equilibrium equation (equation 1 in Appendix) and constitutive laws (see Appendix) are combined, and the system is solved in total stress (cases 1 and 3). Ultimately, when we express results, we merely subtract hydrostatic pore pressure from total stress to present effective stress (case 1). An alternative approach (cases 2 and 4), which assumes that pore pressure is equal to hydrostatic pore pressure, includes it in the governing equations (see equation 2 in Appendix) and solves the system in effective stress. However, when

we include plasticity in the models (case 4), the governing equations must be solved in effective stress (see equation 2 in Appendix).

## MODEL RESULTS

We present four cases (Table 1) to explore deformation and stresses around a spherical salt body having a 1-km (0.6-mi) radius and whose center is located 5 km (3.1 mi) below the top of the model (Figure 1). First, we compare total-stress modeling (case 1) with effective-stress modeling (case 2) in models that have elastic sediments. Next, we introduce the effects of plasticity around a spherical salt body (case 4). We then further consider the impact of different plastic yield criteria (case 4) and compare total-stress modeling (case 3) with effective-stress modeling (case 4) using plasticity. Finally, we extend our analysis to explore deformation and stresses around an irregular salt sheet in the elastoplastic models (case 4).

### Elastic Sediments: Case 1 and Case 2

We begin with an elastic total-stress model (case 1). The final stress state (Figure 2C) is the sum of the imposed initial stress state (Figure 2A) and the stress perturbation that results from viscoelastic stress relaxation of the salt body (Figure 2B). Before salt relaxation, von Mises stress increases everywhere

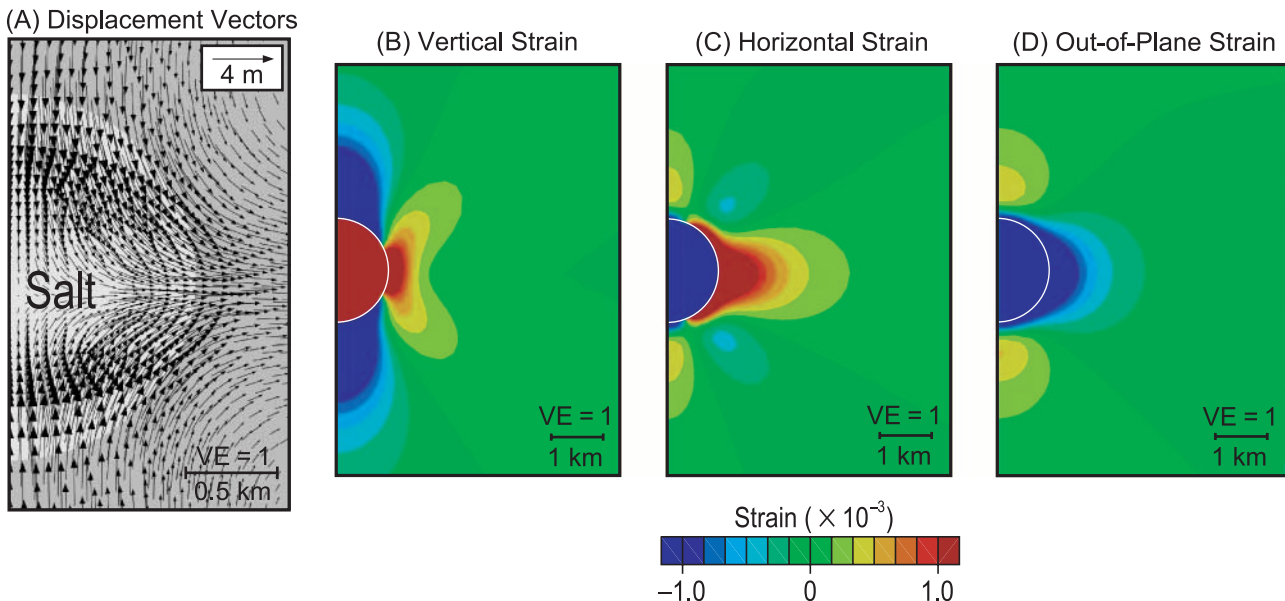


**Figure 3.** The deformation pattern within and around the salt sphere during the processes of salt viscoelastic stress relaxation predicted by the elastic model in case 1: (A) displacement vectors, (B) vertical strain, (C) horizontal strain, and (D) out-of-plane strain. Red is contractional strain (positive) and blue is extensional strain (negative). Note that strain in sediments is elastic, but strain within the salt includes both elastic and viscous strain. The white semicircle is the interface between salt and sediments. This case is the same as that in Figure 2. VE = vertical exaggeration.

with depth because we impose a linearly increasing difference between vertical and horizontal stresses with depth (Figure 2A).

During stress relaxation, salt flows inward from the poles toward the center and outward from the center toward the equator (Figure 3A). Relaxation

of the salt causes vertical extension above and below the salt and vertical contraction (or vertical shortening) at the equator (Figure 3B). Contractional strain is positive in this study. Horizontal contraction (or horizontal shortening) at the equator (Figure 3C) and extensional out-of-plane or hoop

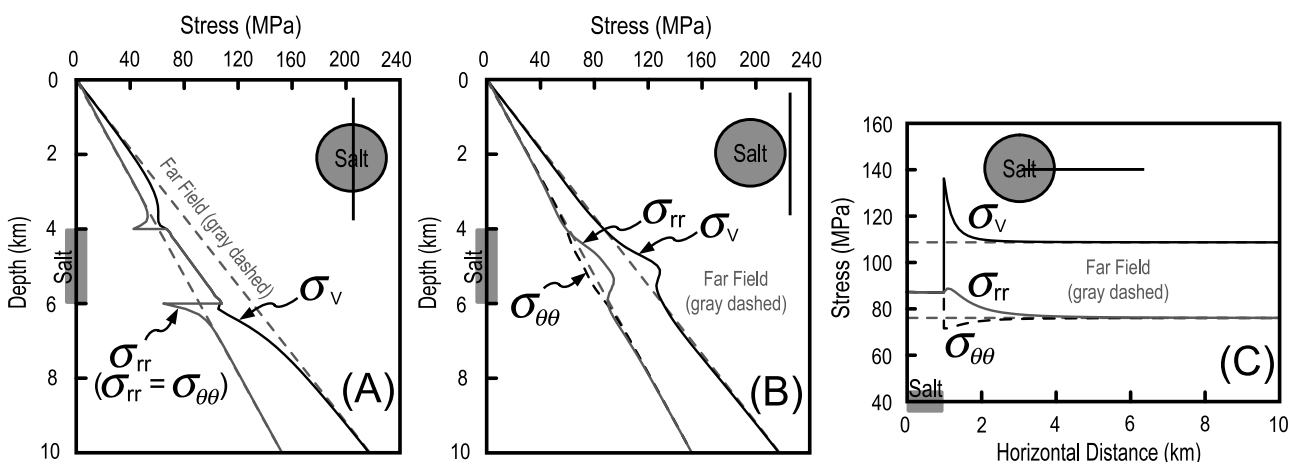


**Figure 4.** Final total stresses for the two vertical profiles through the center of the salt sphere (A) and through the sediments just beyond the edge of the salt sphere (B), and the horizontal profile through the center of the salt sphere (C) predicted by the elastic model in case 1. Compressional stress is positive in this study. Gray dashed lines show far-field horizontal and vertical stresses, respectively. Horizontal stress is equal to out-of-plane stress for the vertical profile through the salt center (A). Salt position is shown on axes. This case is the same as that in Figure 2. Symbols defined in Table 2.

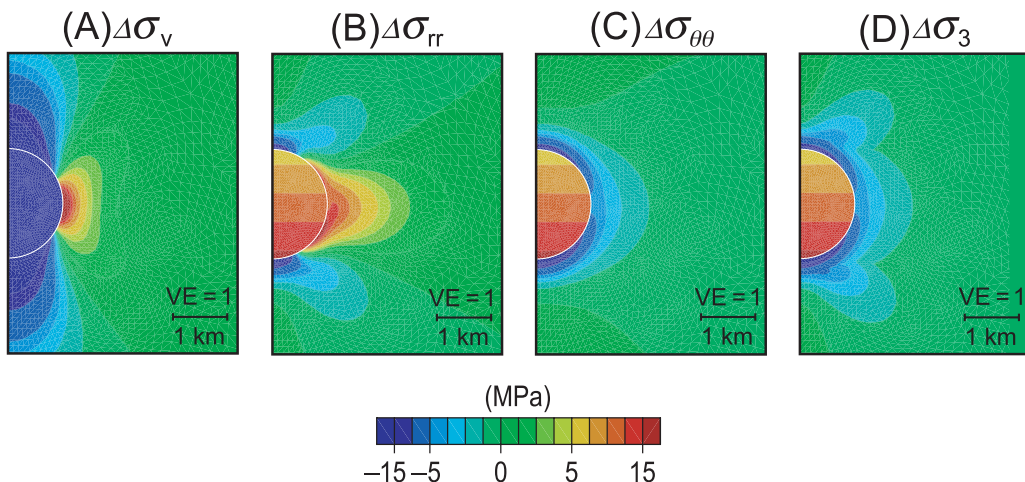


**Figure 5.** Stress perturbations for the salt sphere predicted by the elastic model in case 1: (A) vertical stress, (B) horizontal stress, (C) out-of-plane stress, and (D) minimum principal stress. The white semicircle is the interface between salt and sediments. This case is the same as that in Figure 2. VE = vertical exaggeration.

strain at the equator (Figure 3D) also exist. These cause von Mises stress to increase at the equator of the salt body (lateral edge) and decrease at the poles (top and bottom) (Figure 2B). These perturbations can reach approximately 50% of initial stresses (Figure 2A, B). Finally, after salt stress relaxation, almost no von Mises stress (<0.1 MPa [ $<14.5$  psi]) exists within the salt (Figure 2C).

A vertical profile through the center of the salt body illustrates the changes in stresses caused by salt relaxation (Figure 4A). Compressional stress is positive in this study. Gray dashed lines represent the initial or far-field stress state, whereas solid curves represent the stress state after salt relaxation. As expected, within the salt (between 4- and 6-km [2.5- and 3.7-mi] depth), vertical and horizontal stresses ( $\sigma_v$  and  $\sigma_{rr}$ ) are equal and lie between initial stresses (or far-field stresses). Vertical

and horizontal stresses are reduced just above and below the salt (Figure 4A).

A vertical profile through the sediments just beyond the edge of the salt body illustrates that both vertical and horizontal stresses ( $\sigma_v$  and  $\sigma_{rr}$ ) increase at the equator of the salt body (Figure 4B). A modest decline in the out-of-plane or hoop stress ( $\sigma_{\theta\theta}$ ) exists. Finally, a horizontal profile through the salt illustrates that within the salt, all three stresses are equal. Away from the salt-sediment interface, a sharp increase in vertical stress, a moderate increase in horizontal stresses, but a decline in out-of-plane or hoop stress (Figure 4C) occur.

Spatial distributions of perturbations of vertical stress, horizontal stress, out-of-plane stress, and minimum principal stress ( $\Delta\sigma_v$ ,  $\Delta\sigma_{rr}$ ,  $\Delta\sigma_{\theta\theta}$ , and  $\Delta\sigma_3$ ) are illustrated in Figure 5. Vertical and horizontal stresses decrease above and below the salt

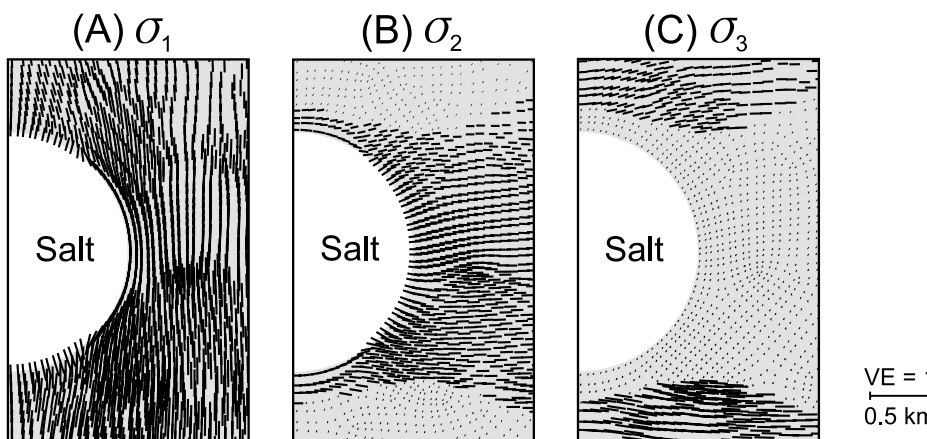
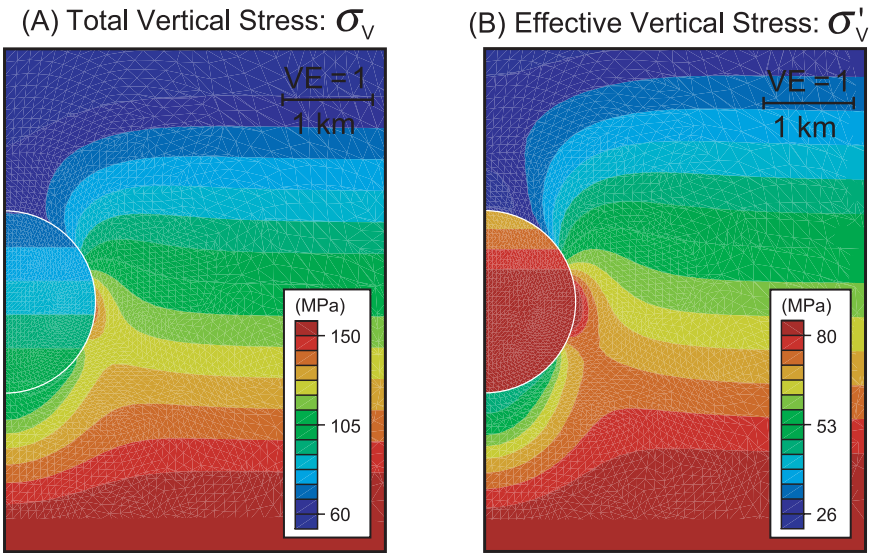


**Figure 6.** Orientations of final principal stresses predicted by the elastic model in case 1: (A) maximum principal stress ( $\sigma_1$ ), (B) intermediate principal stress ( $\sigma_2$ ), and (C) minimum principal stress ( $\sigma_3$ ). Bars show orientations of principal stresses in this plane and dots show the out-of-plane orientation. This case is the same as that in Figure 2. VE = vertical exaggeration.

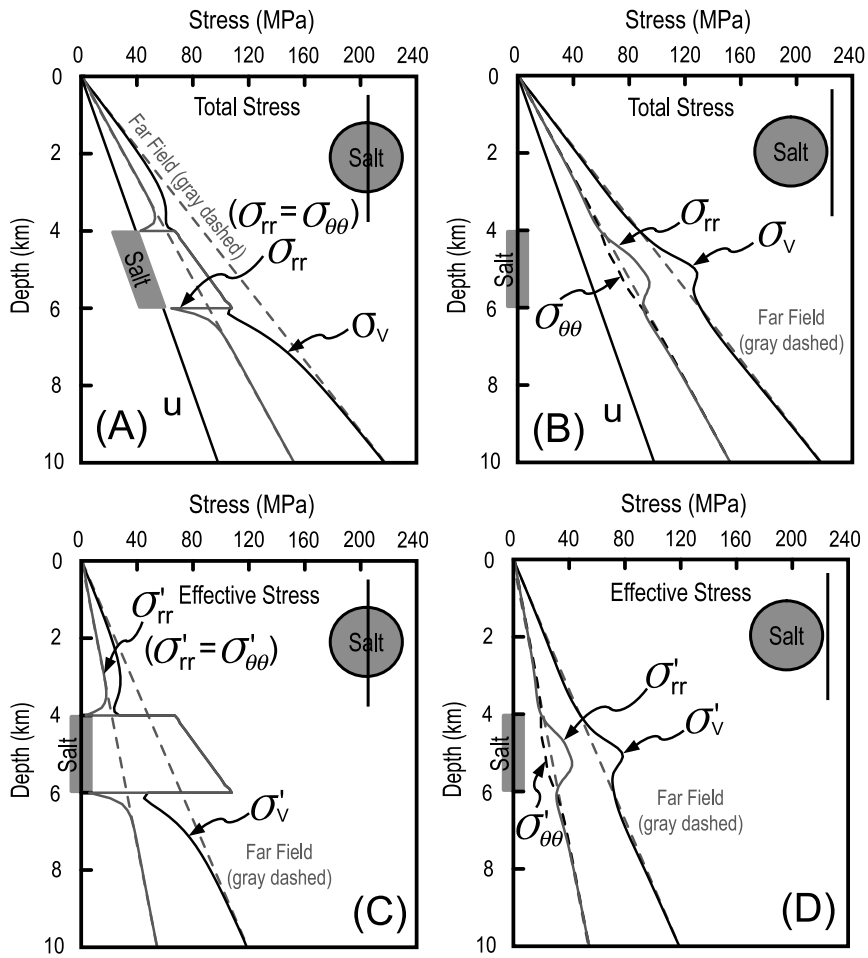
**Figure 7.** Final vertical stress for the salt sphere predicted by elastic models in cases 1 and 2: (A) total stress and (B) effective stress. Effective stresses are calculated from either case 1 or case 2. Effective stresses predicted by the two approaches are equal, and so are total stresses. The white semi-circle is the interface between salt and sediments. The case number is shown in Table 1, and material parameters are shown in Table 3. VE = vertical exaggeration.



sphere and increase at the equator (Figure 5A, B). Out-of-plane and minimum principal stresses are decreased around the salt sphere (Figure 5C, D).

Maximum principal stress ( $\sigma_1$ ) is oriented approximately vertically within the vertical cross section (Figure 6A); however, rotation of maximum

**Figure 8.** Vertical profiles of final stresses through the center of the salt sphere and through the sediments just beyond the edge of the salt sphere predicted by the elastic models in cases 1 and 2: total stresses for the two vertical profiles in (A) and (B), and effective stresses for the two vertical profiles in (C) and (D). Gray dashed lines show far-field horizontal and vertical stresses, respectively. The assumed hydrostatic pore pressure profile is shown in (A) and (B). Effective stresses calculated from case 1 and case 2 are identical. These cases are the same as those in Figure 7. Symbols are defined in Table 2.



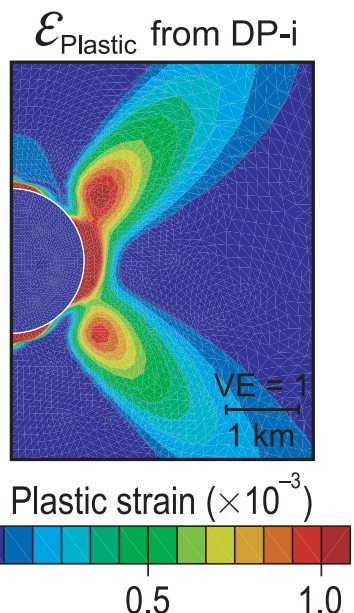


**Figure 9.** Magnitude of plastic strain ( $\epsilon_{\text{plastic}}$ ) predicted by the elastic-perfectly-plastic model using the inner circle of the Drucker-Prager plastic yield criterion (DP-i) in case 4. White semicircle is the interface between salt and sediments. Case number is shown in Table 1 and material parameters are shown in Table 3. VE = vertical exaggeration.

principal stress orientation near the salt is significant. The orientation of intermediate principal stress ( $\sigma_2$ ) is generally horizontal (or radial) within the vertical plane along the equatorial regions of the salt (bars in Figure 6B); however, it is oriented out of the plane above and below the salt (dots in Figure 6B). The orientation of minimum principal stress ( $\sigma_3$ ) is horizontal (or radial) within the vertical plane above and below the salt, whereas it is oriented out of the

plane around the margins of the salt (Figure 6C). Thus, with depth, the orientation of intermediate principal stress rotates from out-of-plane, to horizontal, and then back to out-of-plane orientations (Figure 6B). The orientation of minimum principal stress also rotates from horizontal to out-of-plane and back to horizontal orientations with increasing depth (Figure 6C). These results show that out-of-plane stress near the salt is minimum principal stress and explain that stress changes in Figure 5C and D are equal just around the salt sphere.

Effective stress is total stress minus pore pressure. Because pore pressure is assumed to be hydrostatic, the effective-stress field looks extremely similar to the total-stress plot, although the magnitudes are approximately half (compare Figure 7A, B). The differences in magnitude between total and effective stresses are also illustrated in vertical profiles through the salt body and through the sediments just beyond the edge of the salt (Figure 8). As discussed in the model setup section, the force equilibrium equation can be solved in total stress (see equation 1 in Appendix, case 1), and then hydrostatic pore pressure can be subtracted; or the force equilibrium equation can also be solved in effective stress (see equation 2 in Appendix, case 2). Either way produces identical results (Figures 7, 8). Cases 1 and 2 are thus equivalent.

These results are essentially equivalent to previously published results of relaxation of a salt sphere in an elastic medium (e.g., Fredrich et al., 2003; Koupriantchik et al., 2005; Mackay et al., 2008;

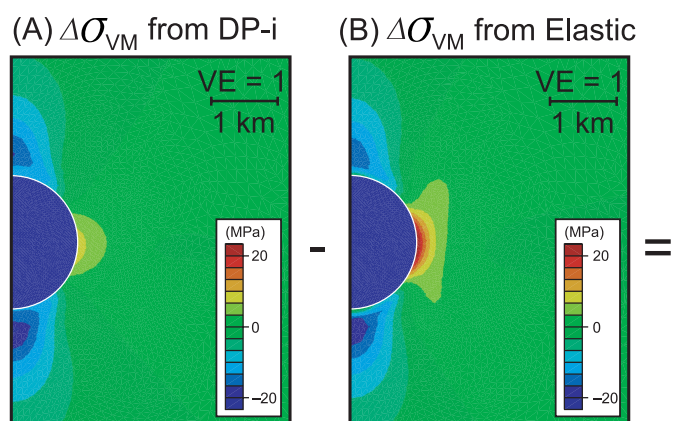
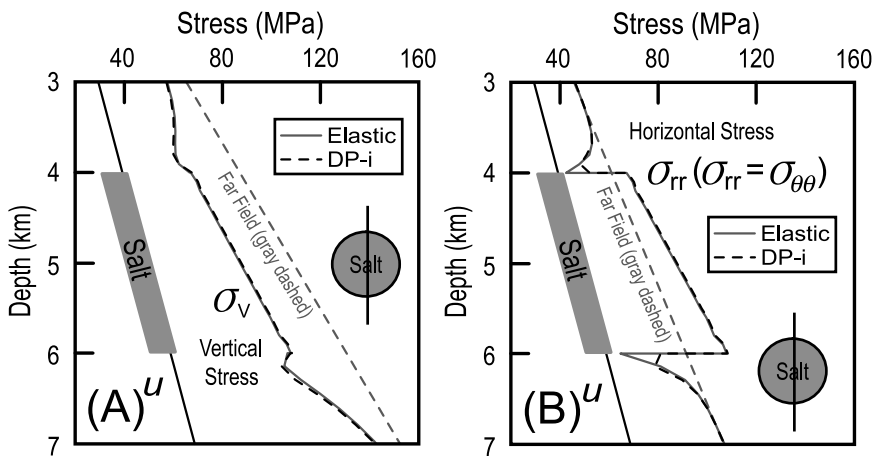


**Figure 10.** Perturbations of von Mises stress ( $\Delta\sigma_{\text{VM}}$ ) predicted by (A) the elastic-perfectly-plastic model using the inner circle of the Drucker-Prager yield criterion (DP-i) in case 4, (B) the elastic model in case 1, and (C) difference in perturbations between the two models. The white semicircle is the interface between salt and sediments. The case number is shown in Table 1 and material parameters are shown in Table 3. VE = vertical exaggeration.

**Figure 11.** Final total stresses for the vertical profile through center of the salt sphere predicted by the elastic-perfectly-plastic model using the inner circle of the Drucker-Prager yield criterion (DP-i) in case 4 and the elastic model in case 1: (A) vertical stress and (B) horizontal stress. Gray dashed lines show far-field horizontal and vertical stresses, respectively. The assumed hydrostatic pore pressure profile is shown. Horizontal stress is equal to out-of-plane stress for this profile. These cases are the same as those in Figure 10. Symbols defined in Table 2.



Sanz and Dasari, 2010). We include them to provide physical insight into the deformation accompanying relaxation of a salt sphere and to provide a point of reference against which to compare the elastoplastic results presented next.

### Elastoplastic Sediments: Case 3 and Case 4

#### Effects of Plasticity

To examine the effects of plasticity, we first compare results from an elastic-perfectly-plastic model (case 4) with those of the elastic model (case 1 = case 2). For this comparison, we use the inner circle of the Drucker-Prager plastic yield criterion (see Appendix) with an effective-stress model, assuming hydrostatic pore pressure in sediments. In per-

fect plasticity, when stresses in sediments reach the yield value, plastic strain will occur. The magnitude of plastic strain is defined by

$$\epsilon_{Plastic} = \sqrt{\frac{2}{3}[(\epsilon_1^{pl})^2 + (\epsilon_2^{pl})^2 + (\epsilon_3^{pl})^2]} \quad (3)$$

where  $\epsilon_1^{pl}$ ,  $\epsilon_2^{pl}$ , and  $\epsilon_3^{pl}$  are three principal components of the plastic strain tensor.

In this example, plastic strain is asymmetric (Figure 9). In general, areas with high von Mises stress in the elastic model (Figure 10B) also have high von Mises stress in the elastoplastic model (Figure 10A). However, final von Mises stress is significantly lower in the elastoplastic model (Figure 10A, B) because sediments yield and plastic laws impose limitations on

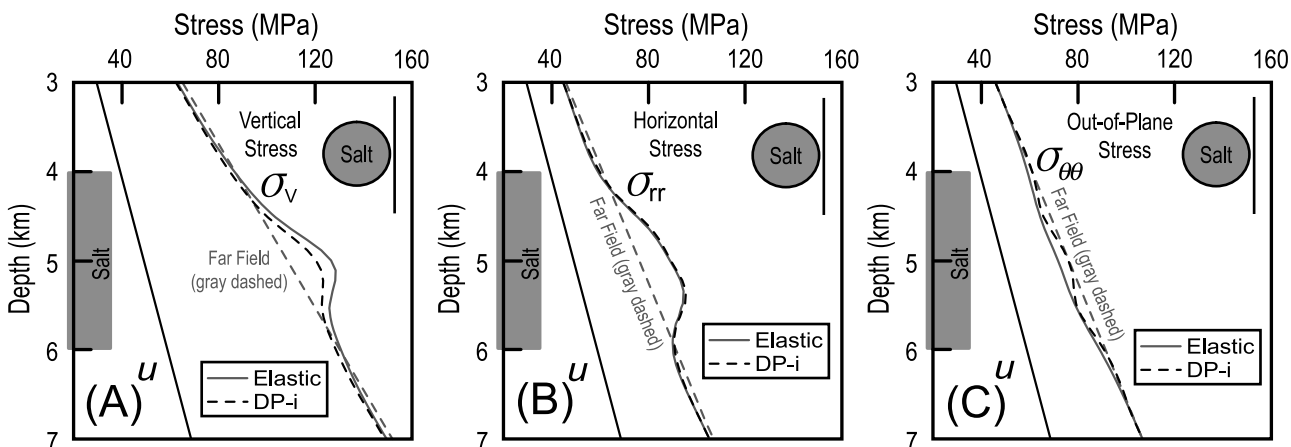


**Figure 12.** Final total stresses for the vertical profile through the sediments just beyond the edge of the salt sphere predicted by the elastic-perfectly-plastic model using the inner circle of the Drucker-Prager yield criterion (DP-i) in case 4 and the elastic model in case 1: (A) vertical stress, (B) horizontal stress, and (C) out-of-plane stress. The assumed hydrostatic pore-pressure profile is shown. The gray dashed lines show far-field horizontal and vertical stresses, respectively. These cases are the same as those in Figure 10. Symbols are defined in Table 2.

differential stresses. The concentration of von Mises stress at the lateral edge of the salt sphere is thus reduced, and stresses are redistributed (Figure 10C).

In a vertical profile through the salt center, vertical stresses predicted by the elastoplastic model just above and below the salt are slightly lower than those of the elastic model (Figure 11A). In contrast, horizontal stresses in the elastoplastic model are higher (~7–15 MPa [~1015–2176 psi]) than those predicted by the elastic model (Figure 11B). In a vertical profile through the sediments just beyond the edge of the salt sphere, the elastoplastic model predicts vertical stresses about 10 MPa (~1450 psi) lower than the elastic model at the salt boundary (Figures 12A, 13A). The elastoplastic model predicts horizontal stresses at the lateral edge slightly higher than the elastic model (Figures 12B, 13B); out-of-plane stresses predicted by the elastoplastic model at the lateral edge are about 4 MPa (~580 psi) higher than those predicted by the elastic model (Figures 12C, 13C). All results show the same effects of plasticity on stresses around the salt sphere: the elastic model has no limit for shear stresses, but the elastoplastic model yields at higher deviatoric stresses, limiting stress levels in the model.

### Impact of Different Plastic Yield Criteria and Modeling Approaches

Different plastic constitutive models have a significant impact on resulting plastic strain distributions and stresses (Figures 14, 15). The inner circle of the Drucker-Prager plastic yield criterion predicts the largest plastic deformation zone and the largest plastic strain magnitude (Figure 14A). The outer circle of the Drucker-Prager plastic yield criterion predicts plastic deformation only above and below the salt sphere, but no plastic strain at the lateral edge of the salt sphere (Figure 14B). The Mohr-Coulomb plasticity shows a plastic deformation zone at the lateral edge and predicts plastic strain intermediate between those from the inner and outer circles of the Drucker-Prager plastic yield criterion (Figure 14C). The inner circle of the Drucker-Prager plastic yield criterion is thus weakest, and the outer circle strongest.

All three elastoplastic constitutive models are effective-stress models (case 4), and the rock fails

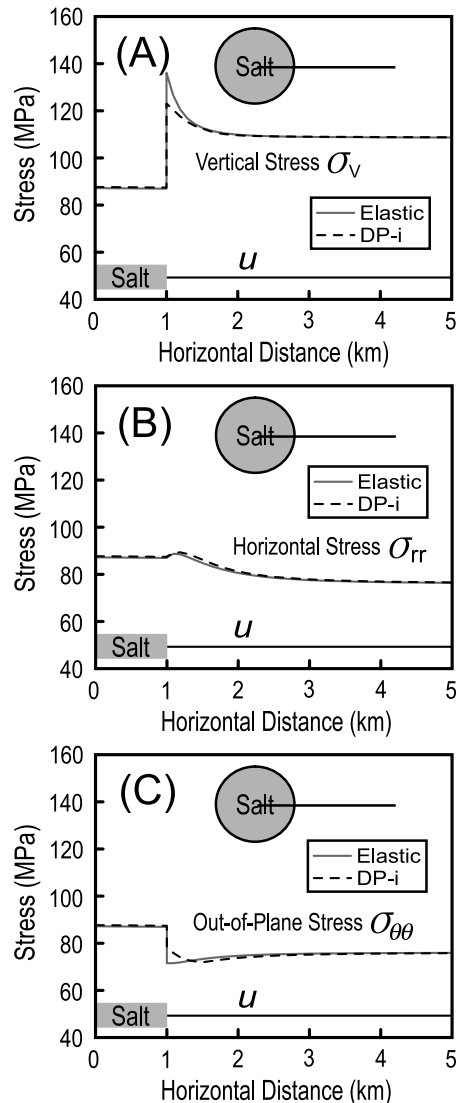


**Figure 13.** Final total stresses for the horizontal profile through the center of the salt sphere predicted by the elastic-perfectly-plastic model using the inner circle of the Drucker-Prager yield criterion (DP-i) in case 4 and the elastic model in case 1: (A) vertical stress, (B) horizontal stress, and (C) out-of-plane stress. The assumed hydrostatic pore pressure profile is shown. These cases are the same as those in Figure 10. Symbols are defined in Table 2.

in shear at a certain effective stress. A different approach, popular among published studies (e.g., Schultz-Ela, 2003), is to modify the internal friction angle and cohesion parameters in a total-stress model (case 3B) to account for the effect of linearly increasing pore pressure with depth. This methodology is detailed in the Appendix for a hydrostatic pore-pressure profile and the Mohr-Coulomb plasticity criterion. A total-stress model (case 3B) with an effective internal friction angle of 15.95° and

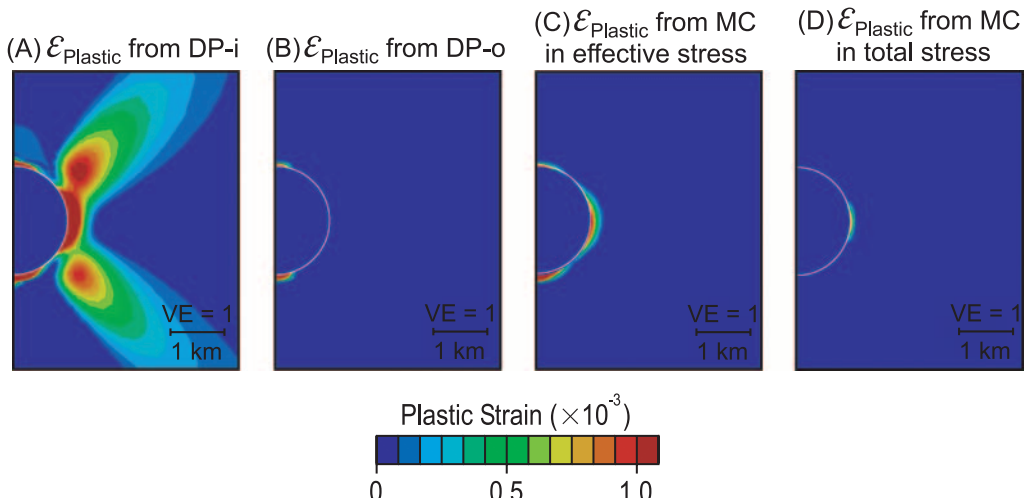


**Figure 14.** Magnitude of plastic strain predicted by different elastic-perfectly-plastic models: (A) the inner circle of the Drucker-Prager yield criterion (DP-i), (B) the outer circle of the Drucker-Prager yield criterion (DP-o), (C) the Mohr-Coulomb yield criterion (MC) in effective-stress modeling in case 4, and (D) the Mohr-Coulomb yield criterion in total-stress modeling with effective internal friction angle and effective cohesion in case 3B. Hydrostatic pore pressure is assumed. An internal friction angle of 30° and cohesion of 0.03 MPa (4.4 psi) are used in (A), (B), and (C). An effective internal friction angle of 15.95° and effective cohesion of 0.027 MPa (3.9 psi) are used in (D). The white semicircle is the interface between salt and sediments. The case number is shown in Table 1 and material parameters are shown in Table 3. VE = vertical exaggeration.

effective cohesion of 0.027 MPa (3.9 psi) is “equivalent” to an effective-stress model (case 4) under hydrostatic pore pressure and with an internal friction angle of 30° and cohesion of 0.03 MPa (4.4 psi) (see equations 10–13 in Appendix). Comparing results from the two modeling approaches, we find

that results from the total-stress system show a smaller plastic strain zone (Figure 14C, D) and more concentration of von Mises stress (Figure 15C, D) than those predicted by the effective-stress system.

The differences between the two modeling approaches are caused by (1) the difference in friction

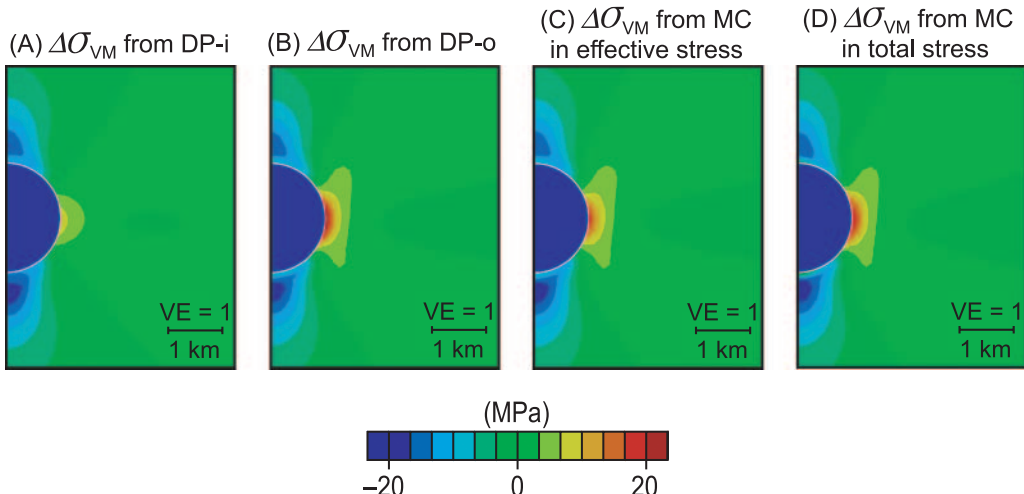


**Figure 15.** Perturbations of von Mises stress predicted by different elastic-perfectly-plastic models: (A) the inner circle of the Drucker-Prager yield criterion (DP-i), (B) the outer circle of the Drucker-Prager yield criterion (DP-o), (C) the Mohr-Coulomb yield criterion (MC) in effective-stress modeling in case 4, and (D) the Mohr-Coulomb yield criterion in total-stress modeling with effective internal friction angle and effective cohesion in case 3B. The white semicircle is the interface between salt and sediments. These cases are the same as those in Figure 14. VE = vertical exaggeration.

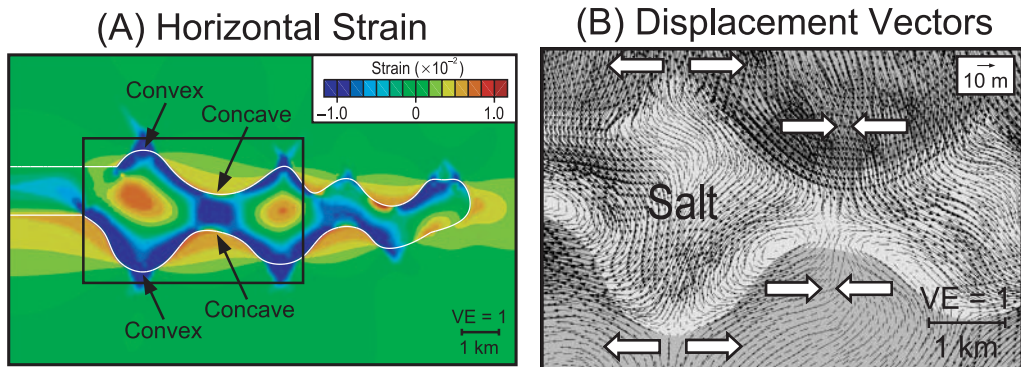


**Figure 16.** Deformation pattern within and around the irregular salt sheet during the processes of viscoelastic stress relaxation predicted by the elastic-perfectly-plastic model with the Mohr-Coulomb plastic yield criterion in case 4: (A) horizontal strain and (B) displacement vectors. Red is contractional strain and blue is extensional strain. Note that strain in sediments includes elastic and plastic strain, but strain within the salt includes elastic and viscous strain. The black box in (A) shows the location of the plot of displacement vectors (B). The white curve is the interface between salt and sediments. The case number is shown in Table 1 and material parameters are shown in Table 3. VE = vertical exaggeration.

angles, which suggests the difference of plastic failure, even for the same stress state, and (2) the assumption that the ratio  $\lambda$  of pore pressure and solid pressure ( $P = \frac{\sigma_1 + \sigma_3}{2}$ ) is equal to Hubbert-Rubey pore-pressure ratio  $\lambda_{\text{HR}}$  (Hubbert and Rubey, 1959; Rubey and Hubbert, 1959), suggesting that solid pressure equals the weight of density-integral overburden (see Appendix), which is unsuitable in this case. The latter is especially true at the two poles and lateral edge of the salt sphere, where solid pressure may deviate from the weight of density-integral overburden (far-field vertical stress) by a wide margin (Figure 4).

In summary, we compare model results from cases 3 and 4. We assume hydrostatic pore pressure in the sediments and include plasticity in the sediments in modeling. Because both the Drucker-Prager and the Mohr-Coulomb plastic yield criteria are commonly used in numerical models for salt systems (e.g., Poliakov et al., 1993a, 1996; Schultz-Ela and Walsh, 2002; Dirkzwager and Dooley, 2008), we also explore and compare effects of different plastic yield criteria: the Drucker-Prager (inner and outer circles) and the Mohr-Coulomb plastic yield criteria in effective-stress models in case 4 (see equations 6–9 in Appendix) and the Mohr-Coulomb plastic yield criterion in a total-stress model in case 3 (see equations 10–13 in Appendix). In short, elasto-plastic models can predict much different results from those by elastic models, and different mod-

eling approaches and different plastic constitutive laws can also predict different results.

#### A Complex Salt Geometry

We additionally explore a more complex salt geometry—an irregular salt sheet—which we solve using an effective-stress approach assuming hydrostatic pore pressure (case 4) in the 2-D axisymmetric model. We use the elastic-perfectly-plastic constitutive law with Mohr-Coulomb plasticity for the sediments.

The outer surface of the irregular salt sheet has an undulating topography (Figure 16A): where the salt is thicker, the outer surface is convex; where it is thinner, the outer surface is concave. Horizontal extension occurs in the sediments adjacent to where the salt surface is convex; in these locations, the salt is vertically contracted and horizontally extended in a manner similar to that of the salt sphere (compare Figures 3, 16). In contrast, a strong horizontal contraction exists in the sediments adjacent to where the salt surface is concave (Figure 16A).

Plastic strain occurs at all convex surfaces of the irregular salt sheet (Figure 17A), and von Mises stress decreases (Figure 17B). The von Mises stress also rises above and below areas where salt is concave (warm colors in Figure 17B). The minimum principal stress, as a proxy for the fracture gradient, is decreased at all locations where the salt surface

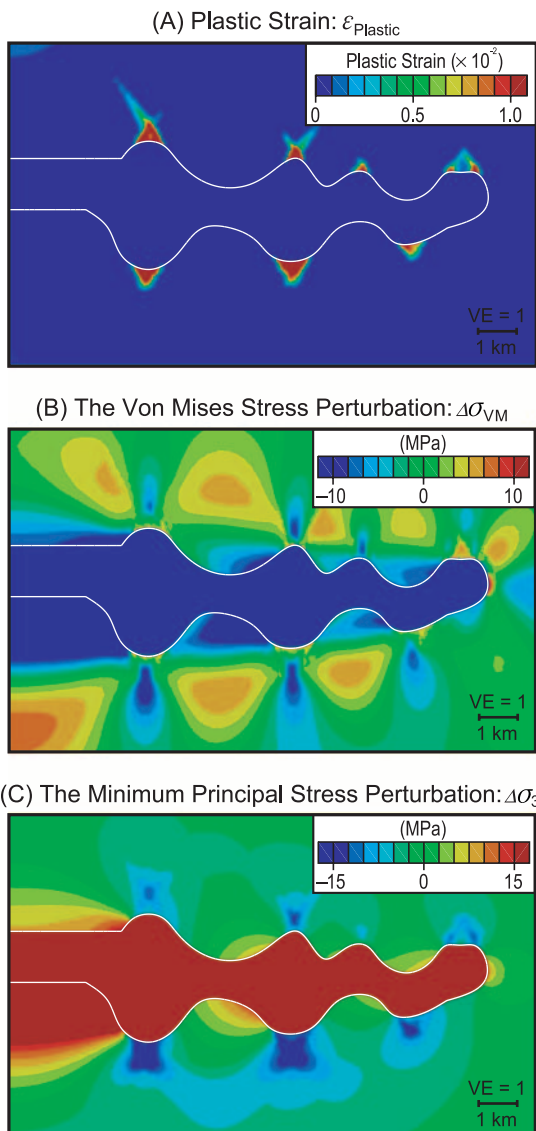


**Figure 17.** (A) Magnitude of plastic strain, (B) perturbations of von Mises stress, and (C) perturbations of minimum principal stress predicted by the elastic-perfectly-plastic model with the Mohr-Coulomb yield criterion in case 4 for the irregular salt sheet. The white curve is the interface between salt and sediments. This case is the same as that in Figure 16. VE = vertical exaggeration.

is convex (cold colors in Figure 17C). However, minimum principal stress is high where the salt surface is concave (Figure 17C).

In this example, mean stress within the salt converges approximately to the vertical stress (Figure 18). The increase in mean stress within the salt causes additional horizontal compression and contraction in the sediments on the left and right sides of where the salt surface is convex (Figures 16, 18). These re-

sults explain why large horizontal contraction occurs (Figure 16A) and horizontal stresses increase where the salt surface is concave (Figure 18B). Our model results are comparable with previously published results of finite-element modeling around an irregular salt sheet (e.g., Fredrich et al., 2007).

## DISCUSSION

### Analysis of Model Results

These results show that elastic and elastoplastic models predict significantly different stresses around salt. Stress perturbations generated by elastoplastic models are less than those generated by elastic models (Figure 10). Differences occur when different plastic yield criteria are used in calculations: the Drucker-Prager inner-circle criterion produces a large plastic strain in our example, whereas the Drucker-Prager outer-circle criterion creates only small amounts of plastic strain. Elastoplastic models have previously been applied to salt basin evolution and deformation modeling around salt (e.g., Schultz-Ela and Walsh, 2002; Schultz-Ela, 2003; Dirkzwager and Dooley, 2008). Plasticity will better simulate stress perturbations around salt bodies, which are known to involve plastic deformation in nature (e.g., Ratcliff et al., 1992; Davison et al., 2000b; Schultz-Ela, 2003).

The choice of initial stress field can impact modeling results. We choose to represent the basin in a state of uniaxial strain or under  $K_0$  conditions. This is suitable for geologic environments, in which stresses are generated primarily by depositional processes. However, many different far-field stresses can be assumed. For example, salt structures can also exist in environments of horizontal compression or extension (e.g., Jackson et al., 1994; Stefanescu et al., 2000). An alternative approach would be to assume a critically stressed system, either in extension or compression (e.g., Zoback, 2007).

All of the models show the same general stress and deformation patterns around a relaxing salt sphere. The salt shortens vertically and expands laterally, producing zones of extension at the top and base of the sphere and a zone of shortening

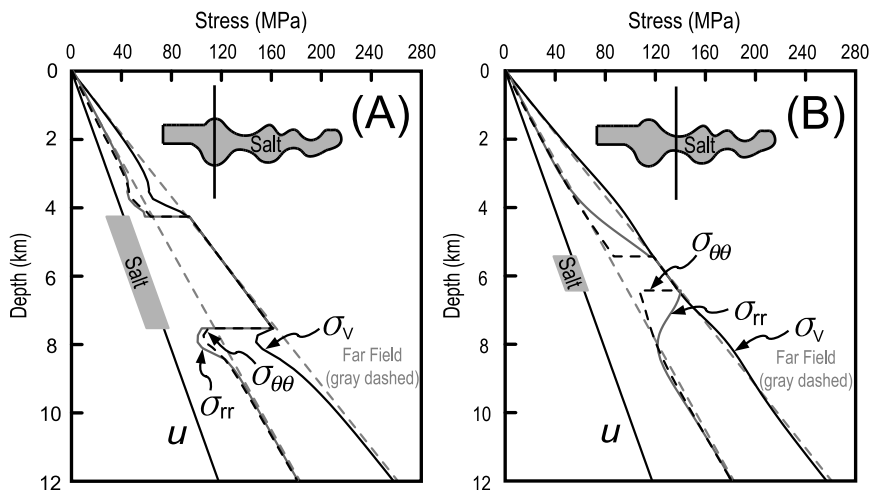


**Figure 18.** Final total stresses for two vertical profiles through the irregular salt sheet predicted by the elastic-perfectly-plastic model with the Mohr-Coulomb yield criterion in case 4: (A) the profile through salt convex curves and (B) the profile through salt concave curves. The gray dashed lines show far-field horizontal and vertical stresses, respectively. The assumed hydrostatic pore pressure profile is shown. This case is the same as that in Figure 16. Symbols defined in Table 2.

around the equator of the sphere. In accordance with this deformation, vertical, radial, and hoop stresses are all reduced at the top and bottom of the sphere. Vertical and radial stresses are both increased around the equator of the sphere, accompanied by a minor reduction in hoop stress. Finally, principal stresses are rotated near the salt, so that they are no longer necessarily horizontal or vertical. In the ideal situation of a fully relaxed salt body, deviatoric stresses are zero within the salt, and because of stress continuity at the salt interface, one of the principal stresses at the salt interface is always oriented normal to the salt surface and the other two principal stresses are within the salt-sediment interface (Figure 6).

### Comparison with Previous Work

This stress pattern around a salt sphere is analogous to the pattern of stress distribution around a cavity in an elastic material (e.g., Kirsch, 1898; Timoshenko and Goodier, 1970). When a hole or tunnel is created, bridging occurs: horizontal and vertical tension occurs above and below the hole, whereas horizontal and vertical compression occurs at the lateral edges of the hole (e.g., Hoek and Brown, 1996). In our models, a reduction of vertical stresses above and below the salt sphere causes stress redistribution around the salt, and as a result, these stresses increase along the equator (Figure 5A). This approach has been applied as a way of explaining borehole stresses (e.g., Peska and Zoback, 1995;

Zoback, 2007) and underground excavation and tunneling problems (e.g., Hoek and Brown, 1996).

The pattern of stresses that we have modeled is consistent with that of stresses encountered around natural salt bodies. For example, Rohleder et al. (2003) showed the observed gradient decrease in minimum principal stress below salt, and others have reported lost circulation above salt, suggesting low minimum principal stress (e.g., Bradley, 1978; Whitson and McFadyen, 2001; Dusseault et al., 2004). These observations are consistent with our predicted stresses (e.g., Figures 4A, 18A). Our models thus suggest that lateral spreading of salt may be a cause of low minimum principal stress encountered above and below salt in many wells. Radial and concentric extensional faults near the salt diapir have been observed and reported (e.g., Davison et al.,

### Extensional Fault Pattern

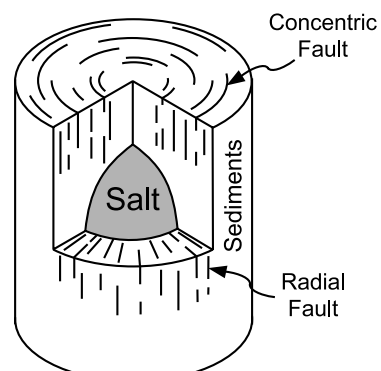


**Figure 19.** Cartoon showing extensional fault patterns around salt sphere predicted by our models.

2000a, b; Dusseault et al., 2004). The pattern of our model stresses near the salt sphere (Figure 6) suggests these extensional faults (Figure 19).

## Practical Implications

In the irregular salt sheet that we simulate, minimum principal stress drops where salt is thick (at convex salt surfaces), but not where salt is thin (at concave salt surfaces) (Figure 17C), suggesting that a more stable drilling path may lie where the salt surface is concave. On the basis of our modeling and other numerical experiments (e.g., Fredrich et al., 2003), we find that mean stress within salt converges toward far-field vertical stress for those salt bodies that are wide and thin (e.g., a salt sheet), whereas mean stress converges approximately to far-field horizontal stress when salt bodies are narrow and tall (e.g., a salt dome); salt bodies with a more equal aspect ratio, such as the salt sphere, have mean stress roughly converging to the far-field mean stress.

Modeling of stresses around salt will, ultimately, be fully coupled in the sense that pore pressure and fluid flow will be coupled to sediment deformation induced by salt behavior (Nikolinakou et al., 2012), and future models will simulate the geologic evolution of these systems. In systems with plasticity (unlike elastic models), because the history of deformation will impact the final state, modeling their evolution will become critical. The elastoplastic simulations that we have presented herein provide the needed insight into stresses and deformation around salt systems.

## CONCLUSIONS

1. Elastoplastic models of sediments can simulate stresses around salt more realistically than elastic models. Elastic models induce unrealistically large shear stress and unrealistically low minimum principal stress at salt boundaries. In contrast, plastic yielding in elastoplastic models keeps shear stress lower.
2. Large deviatoric stresses (or von Mises stress) are concentrated at the lateral edge of a salt sphere,

mean stress is dropped above and below the salt sphere, and minimum principal stress is lowered everywhere around the salt sphere.

3. A model of an irregular salt sheet shows that mean stress within the salt converges to the far-field vertical stress and that minimum principal stress is lowest where the salt is thick.
4. By providing insight as to where increased and suppressed magnitudes of minimum principal stress (fracture gradient) are expected, this study has implications for drilling near salt bodies.

## APPENDIX

### Force Equilibrium Equation

Using the commercial finite-element analysis software, Abaqus, we solve the force equilibrium equation for the axisymmetric problem in cylindrical coordinate system of  $(r, \theta, z)$ . We can solve the equation in either total stress (equation 1) or effective stress (equation 2):

$$\begin{cases} \frac{\partial \sigma_{rr}}{\partial r} + \frac{\partial \sigma_{rz}}{\partial z} + \frac{\sigma_{rr} - \sigma_{\theta\theta}}{r} = 0 \\ \frac{\partial \sigma_{rz}}{\partial r} + \frac{\partial \sigma_{zz}}{\partial z} + \frac{\sigma_{rz}}{r} + f_z = 0 \\ \sigma_{r\theta} = \sigma_{z\theta} = 0 \end{cases} \quad (1)$$

$$\begin{cases} \frac{\partial (\sigma'_{rr} + u)}{\partial r} + \frac{\partial \sigma'_{rz}}{\partial z} + \frac{\sigma'_{rr} - \sigma'_{\theta\theta}}{r} = 0 \\ \frac{\partial \sigma'_{rz}}{\partial r} + \frac{\partial (\sigma'_{zz} + u)}{\partial z} + \frac{\sigma'_{rz}}{r} + f_z = 0 \\ \sigma'_{r\theta} = \sigma'_{z\theta} = 0 \end{cases} \quad (2)$$

where  $\{\sigma\} = [\sigma_{rr} \sigma_{zz} \sigma_{\theta\theta} \sigma_{rz} \sigma_{r\theta} \sigma_{z\theta}]^T$  is the total stress vector,  $\{\sigma'\} = [\sigma'_{rr} \sigma'_{zz} \sigma'_{\theta\theta} \sigma'_{rz} \sigma'_{r\theta} \sigma'_{z\theta}]^T$  is the effective-stress vector,  $u$  is pore pressure,  $f_z = \rho g$  is gravitational body force,  $\rho$  is bulk density of sediments or salt bodies, and  $g$  is gravitational acceleration. The relation between total stress  $\sigma_{ij}$ , effective stress  $\sigma'_{ij}$ , and pore pressure  $u$  can be expressed as  $\sigma'_{ij} = \sigma_{ij} - \delta_{ij}u$  ( $i, j = r, \theta, z$ ) (Terzaghi, 1925). The last two components in both total-stress vector and effective-stress vector are zero. Here compressional stress is positive.

### Constitutive Laws for Sediments

For elastic sediments, the constitutive equation is Hooke's law (e.g., Timoshenko and Goodier, 1970; Zoback, 2007). When we consider solid material (case 1), we express Hooke's law in terms of total stress. However, when pore pressure is considered (case 2), we express Hooke's law with effective stress.

For elastoplastic sediments, we consider Mohr-Coulomb plasticity and Drucker-Prager plasticity (e.g., McLean and Addis, 1990; Wood, 1990; Dunne and Petrinic, 2005; Zoback,

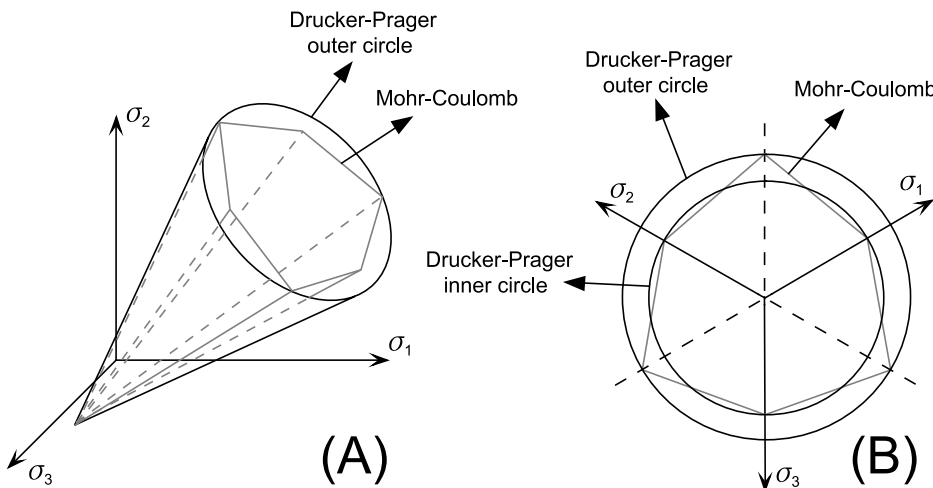


**Figure 20.** The Mohr-Coulomb and the Drucker-Prager plastic yield criteria in the principal stress space (A) and  $\pi$  plane (B). Symbols are defined in Table 2.

2007). Similarly, if the material is considered solid (case 3), these laws are written in terms of total stress, whereas if the presence of pore pressure is included (case 4), the laws must be expressed in terms of effective stress.

### Maxwell Linear Viscoelastic Constitutive Law

We simulate salt using a Maxwell linear viscoelastic body, which is similar to that of previous studies (e.g., Schultz-Ela and Walsh, 2002; Schultz-Ela, 2003; Koupriantchik et al., 2005). Incremental strain includes elastic and viscous components:

$$\{d\epsilon\} = \{d\epsilon^e\} + \{d\epsilon^v\} \quad (3)$$

Incremental elastic strain is given by the elastic Hooke's law (e.g., Timoshenko and Goodier, 1970), and incremental viscous strain is given in equation 4 (e.g., Li et al., 2009; Luo and Liu, 2009, 2010):

$$\{d\epsilon^v\} = [Q]^{-1}\{\sigma^t\}dt, \quad (4)$$

$$[Q]^{-1} = \frac{1}{\eta} \begin{bmatrix} \frac{1}{3} & \frac{1}{6} & \frac{1}{6} & 0 & 0 & 0 \\ -\frac{1}{6} & \frac{1}{3} & -\frac{1}{6} & 0 & 0 & 0 \\ -\frac{1}{6} & -\frac{1}{6} & \frac{1}{3} & 0 & 0 & 0 \\ 0 & 0 & 0 & 1 & 0 & 0 \\ 0 & 0 & 0 & 0 & 1 & 0 \\ 0 & 0 & 0 & 0 & 0 & 1 \end{bmatrix}, \quad (5)$$

where  $[Q]$  is the material matrix in viscosity  $\eta$ ,  $\{\sigma^t\} = [\sigma_r^t \sigma_{zz}^t \sigma_{\theta\theta}^t \sigma_{rz}^t \sigma_{r\theta}^t \sigma_{z\theta}^t]^T$  is total-stress vector at time  $t$ , and  $dt$  is the time increment.

### Plastic Yield Criteria

We apply both the Drucker-Prager and the Mohr-Coulomb plastic yield criteria:  $F_{DP}$  and  $F_{MC}$  (equations 6–9) in the modeling (Abaqus, 2009). We also compare two Drucker-Prager plastic yield criteria: the inner circle of the Drucker-Prager plastic criterion circumscribes the Mohr-Coulomb plas-

tic yield surface, and the outer circle of the Drucker-Prager plastic criterion inscribes it in the principal stress space and the  $\pi$  plane (Figure 20). Here, nonassociated plastic flow rules are used in the modeling.

$$F_{DP} = \sqrt{J_2} - \alpha I'_1 - \beta \quad (6)$$

$$\begin{aligned} \alpha_1 &= \frac{2 \sin \phi}{\sqrt{3}(3 + \sin \phi)} \\ \beta_1 &= \frac{6C \cos \phi}{\sqrt{3}(3 + \sin \phi)} \\ \alpha_2 &= \frac{2 \sin \phi}{\sqrt{3}(3 - \sin \phi)} \\ \beta_2 &= \frac{6C \cos \phi}{\sqrt{3}(3 - \sin \phi)} \end{aligned} \quad (7)$$

$$F_{MC} = \left[ \sin\left(\theta + \frac{\pi}{3}\right) + \frac{\sqrt{3}}{3} \cos\left(\theta + \frac{\pi}{3}\right) \sin \phi \right] \sqrt{J_2} - \frac{\sin \phi}{3} I'_1 - C \cos \phi \quad (8)$$

$$\theta = \frac{1}{3} \cos^{-1} \left( \frac{3\sqrt{3}J_3}{2J_2^{\frac{3}{2}}} \right) \quad (9)$$

where  $I'_1$  is the first invariant of effective-stress tensor,  $J_2$  and  $J_3$  are the second and third invariants of deviatoric stress tensor, respectively,  $\phi$  is internal friction angle,  $C$  is cohesion, and  $\theta$  is the deviatoric polar angle. The  $\alpha_1$  and  $\beta_1$  and  $\alpha_2$  and  $\beta_2$  in equation 7 are two groups of parameters for the inner and outer circles of the Drucker-Prager plastic yield criterion, respectively (e.g., McLean and Addis, 1990). Here, compressional stress is positive.

### Simulating Effect of Pore Pressure by Reducing Internal Friction Angle

This approach has been used widely in previous studies (e.g., Schultz-Ela, 2003; Ings et al., 2004; Gemmer et al., 2005). We use 2-D Mohr-Coulomb plasticity as an example to describe

the approach. The Mohr-Coulomb plastic yield criterion can be given by

$$F_{MC} = \frac{1}{2}(\sigma_1 - \sigma_3) - \left[ \frac{1}{2}(\sigma_1 + \sigma_3) - u \right] \sin \phi - C \cos \phi \quad (10)$$

where  $\sigma_1$  and  $\sigma_3$  are maximum and minimum principal total stresses,  $u$  is pore pressure,  $\phi$  is internal friction angle, and  $C$  is cohesion. Pore pressure is commonly assumed to be equal to  $\lambda P$  ( $u = \lambda P$ ), where  $P$  is solid pressure ( $P = \frac{\sigma_1 + \sigma_3}{2}$ ) and  $\lambda$  is the ratio of pore pressure and solid pressure (e.g., Gemmer et al., 2004, 2005; Ings et al., 2004). The Mohr-Coulomb plastic yield criterion can be changed to

$$\begin{aligned} F_{MC} &= \frac{1}{2}(\sigma_1 - \sigma_3) - \frac{1}{2}(\sigma_1 + \sigma_3)(1 - \lambda) \sin \phi - C \cos \phi \\ &= \frac{1}{2}(\sigma_1 - \sigma_3) - \frac{1}{2}(\sigma_1 + \sigma_3) \sin \phi_{eff} - C_{eff} \cos \phi_{eff} \end{aligned} \quad (11)$$

where  $\phi_{eff}$  and  $C_{eff}$  are the effective internal friction angle and effective cohesion, respectively, and they are given as

$$\begin{aligned} \sin \phi_{eff} &= (1 - \lambda) \sin \phi \\ C_{eff} \cos \phi_{eff} &= C \cos \phi \end{aligned} \quad (12)$$

Here, we assume that  $\lambda$  is equal to Hubbert-Rubey pore-pressure ratio  $\lambda_{HR}$ , and under the conditions of hydrostatic pore pressure, they are given in the equation (Hubbert and Rubey, 1959; Rubey and Hubbert, 1959)

$$\lambda = \lambda_{HR} = \frac{\rho_w}{\rho_{sed}} \quad (13)$$

where  $\rho_w$  is fluid density and  $\rho_{sed}$  is fluid-saturated bulk density of sediments. General values for  $\phi$  and  $C$  in a wet or effective-stress system,  $30^\circ$  and 0.03 MPa (4.4 psi), are “equivalent” to  $15.95^\circ$  and 0.027 MPa (3.9 psi) for  $\phi_{eff}$  and  $C_{eff}$  in a dry or total-stress system ( $\rho_w = 1000 \text{ kg/m}^3$  and  $\rho_{sed} = 2220 \text{ kg/m}^3$ ). If noncohesive sediments are assumed in the modeling ( $C = 0$ ), as done in previous articles (e.g., Gemmer et al., 2005), cohesion-related terms in these equations become zero.

## Initial Stress Field in Modeling

To impose the initial stress field, we assume that vertical stress ( $\sigma_V$ ) is the maximum principal stress and that it can be calculated by integrating bulk densities of the sediments and salt bodies to the depth at any given point:

$$\sigma_V = \rho g z \quad (14)$$

where  $\rho$  is the density of sediments or salt bodies,  $g$  is gravitational acceleration, and  $z$  is depth. The total-stress ratio ( $K_0^T$ ) is expressed as

$$K_0^T = \frac{\sigma_H}{\sigma_V} \quad (15)$$

and the effective-stress ratio is

$$K_0 = \frac{\sigma'_H}{\sigma'_V} = \frac{\sigma_H - u}{\sigma_V - u} \quad (16)$$

Hydrostatic pore fluid pressure is found by integrating fluid density:

$$u = \rho_w g z \quad (17)$$

To determine the relationship between  $K_0^T$  and  $K_0$  for sediments, we substitute equations 14, 15, and 17 into equation 16:

$$K_0 = \frac{K_0^T \rho - \rho_w}{\rho - \rho_w}. \quad (18)$$

We assume that salt bodies are impermeable and have no pore pressure, so in salt bodies,  $K_0^T$  and  $K_0$  are equal.

In our total-stress modeling approach (Table 1), we assume that  $K_0^T$ , the total-stress ratio, is equal to 0.7 in both sediments and salt bodies, and thus, by equation 18, this value equals  $K_0$  with 0.454 in sediments and 0.7 remaining in the salt bodies. These values,  $K_0$  of 0.454 in sediments and  $K_0$  (or  $K_0^T$ ) of 0.7 in the salt bodies, are applied in our effective-stress modeling approach (Table 1).

## REFERENCES CITED

- Bowers, G. L., 2007, Effect of inelastic sediment behavior on near-salt stresses and pore pressures: The Leading Edge, v. 26, p. 1462–1465, doi:[10.1190/1.2805767](https://doi.org/10.1190/1.2805767).
- Bradley, W. B., 1978, Borehole failure near salt domes: Society of Petroleum Engineers Annual Fall Technical Conference and Exhibition, Houston, Texas, October 1–3, 1978, American Institute of Mining, Metallurgical, and Petroleum Engineers, Inc., Paper 7503, 8 p.
- Daudré, B., and S. Cloetingh, 1994, Numerical modeling of salt diapirism: Influence of the tectonic regime: Tectonophysics, v. 240, p. 59–79, doi:[10.1016/0040-1951\(94\)90264-X](https://doi.org/10.1016/0040-1951(94)90264-X).
- Davison, I., G. I. Alsop, P. Birch, C. Elders, N. Evans, H. Nicholson, P. Rorison, D. Wade, J. Woodward, and M. Young, 2000a, Geometry and late-stage structural evolution of Central Graben salt diapirs, North Sea: Marine and Petroleum Geology, v. 17, p. 499–522, doi:[10.1016/S0264-8172\(99\)00068-9](https://doi.org/10.1016/S0264-8172(99)00068-9).
- Davison, I., G. I. Alsop, N. G. Evans, and M. Safaricz, 2000b, Overburden deformation patterns and mechanisms of salt diapir penetration in the Central Graben, North Sea: Marine and Petroleum Geology, v. 17, p. 601–618, doi:[10.1016/S0264-8172\(00\)00011-8](https://doi.org/10.1016/S0264-8172(00)00011-8).
- Dirkzwager, J. B., and T. P. Dooley, 2008, In-situ stress modeling of a salt-based gravity driven thrust belt in a passive margins setting using physical and numerical modeling: The 42nd U.S. Rock Mechanics Symposium (USRMS),

- San Francisco, California, June 29–July 2, 2008, American Rock Mechanics Association Paper 08-270, 6 p.
- Dunne, F., and N. Petrinic, 2005, Introduction to computational plasticity: Oxford, Oxford University Press, 241 p.
- Dusseault, M. B., V. Maury, F. Sanfilippo, and F. J. Santarelli, 2004, Drilling around salt: Risks, stresses, and uncertainties: Gulf Rocks 2004, 6th North America Rock Mechanics Symposium (NARMS), Houston, Texas, June 5–9, 2004, American Rock Mechanics Association Paper 04-647, 12 p.
- Fredrich, J. T., D. Coblenz, A. F. Fossum, and B. J. Thorne, 2003, Stress perturbations adjacent to salt bodies in the deep-water Gulf of Mexico: Society of Petroleum Engineers Annual Technical Conference and Exhibition, Denver, Colorado, October 5–8, 2003, SPE Paper 84554, 14 p.
- Fredrich, J. T., B. P. Engler, J. A. Smith, E. C. Onyia, and D. N. Tolman, 2007, Predrill estimation of subsalt fracture gradient: Analysis of the spa prospect to validate nonlinear finite element stress analyses: Society of Petroleum Engineers/International Association of Drilling Contractors Drilling Conference, Amsterdam, Netherlands, February 20–22, 2007, SPE Paper 105763, 8 p.
- Gemmer, L., S. J. Ings, S. Medvedev, and C. Beaumont, 2004, Salt tectonics driven by differential sediment loading: Stability analysis and finite-element experiments: Basin Research, v. 16, p. 199–218, doi:10.1111/j.1365-2117.2004.00229.x.
- Gemmer, L., C. Beaumont, and S. J. Ings, 2005, Dynamic modeling of passive margin salt tectonics: Effects of water loading, sediment properties and sedimentation patterns: Basin Research, v. 17, p. 383–402, doi:10.1111/j.1365-2117.2005.00274.x.
- Gil, J. A., and M. J. Jurado, 1998, Geological interpretation and numerical modeling of salt movement in the Barbastro-Balaguer anticline, southern Pyrenees: Tectonophysics, v. 293, p. 141–155, doi:10.1016/S0040-1951(98)00097-3.
- Hoek, E., and E. T. Brown, 1996, Underground excavations in rock: London, Spon Press, 536 p.
- Hubbert, M. K., and W. W. Rubey, 1959, Role of fluid pressure in mechanics of overthrust faulting: I. Mechanics of fluid-filled porous solids and its application to overthrust faulting: Geological Society of America Bulletin, v. 70, p. 115–166, doi:10.1130/0016-7606(1959)70[115:ROFPIM]2.0.CO;2.
- Ings, S. J., C. Beaumont, and L. Gemmer, 2004, Numerical modeling of salt tectonics on passive continental margins: Preliminary assessment of the effects of sediment loading, buoyancy, margin tilt, and isostasy: 24th Annual Gulf Coast Section-SEPM Foundation Bob F. Perkins Research Conference, p. 36–68.
- Jackson, M. P. A., B. C. Vendeville, and D. D. Schultz-Ela, 1994, Structural dynamics of salt systems: Annual Review of Earth and Planetary Sciences, v. 22, p. 93–117, doi:10.1146/annurev.ea.22.050194.000521.
- Jaeger, J. C., N. G. W. Cook, and R. W. Zimmerman, 2007, Fundamentals of rock mechanics: Malden, Massachusetts, Blackwell Publishing, 475 p.
- Kirsch, G., 1898, Die Theorie der Elastizität und die Bedürfnisse der Festigkeitslehre: Zeitschrift des Vereines deutscher Ingenieure, v. 42, p. 797–807.
- Koupriantchik, D., S. P. Hunt, P. J. Boult, and A. G. Meyers, 2005, Geomechanical modeling of salt diapirs: Generic shapes and a 3-D salt structure from the Officer Basin, South Australia: Proceedings of the 11th International Conference on Computer Methods and Advances in Geomechanics, Torino, Italy, June 19, 2005, p. 1–9.
- Li, Q., M. Liu, and H. Zhang, 2009, A 3-D viscoelastoplastic model for simulating long-term slip on non-planar faults: Geophysical Journal International, v. 176, p. 293–306, doi:10.1111/j.1365-246X.2008.03962.x.
- Luo, G., and M. Liu, 2009, How does trench coupling lead to mountain building in the Subandes? A viscoelastoplastic finite element model: Journal of Geophysical Research, v. 114, p. 1–16, doi:10.1029/2008JB005861.
- Luo, G., and M. Liu, 2010, Stress evolution and fault interactions before and after the 2008 Great Wenchuan earthquake: Tectonophysics, v. 491, p. 127–140, doi:10.1016/j.tecto.2009.12.019.
- Mackay, F., N. Inoue, S. A. B. Fontoura, and F. Botelho, 2008, Geomechanical effects of a 3-D vertical salt well drilling by FEA: The 42nd U.S. Rock Mechanics Symposium (USRMS), San Francisco, California, June 29–July 2, 2008, American Rock Mechanics Association Paper 08-041, 10 p.
- McLean, M. R., and M. A. Addis, 1990, Wellbore stability: The effect of strength criteria on mud weight recommendations: Society of Petroleum Engineers Annual Technical Conference and Exhibition, New Orleans, Louisiana, September 23–26, 1990, SPE Paper 20405, 9 p.
- Nikolinakou, M. A., G. Luo, M. R. Hudec, and P. B. Flemings, 2012, Geomechanical modeling of stresses adjacent to salt bodies: 2. Poroviscoelasticity and coupled overpressures: AAPG Bulletin, v. 96, p. 65–85.
- Peska, P., and M. D. Zoback, 1995, Compressive and tensile failure of inclined well bores and determination of in situ stress and rock strength: Journal of Geophysical Research, v. 100, p. 12,791–12,811.
- Podladchikov, Y., C. Talbot, and A. N. B. Poliakov, 1993, Numerical models of complex diapirs: Tectonophysics, v. 228, p. 189–198, doi:10.1016/0040-1951(93)90340-P.
- Poliakov, A. N. B., Y. Y. Podladchikov, and C. Talbot, 1993a, Initiation of salt diapirs with frictional overburdens: Numerical experiments: Tectonophysics, v. 228, p. 199–210, doi:10.1016/0040-1951(93)90341-G.
- Poliakov, A. N. B., R. Van Balen, Y. Podladchikov, B. Daudre, S. Cloetingh, and C. Talbot, 1993b, Numerical analysis of how sedimentation and redistribution of surficial sediments affects salt diapirism: Tectonophysics, v. 226, p. 199–216, doi:10.1016/0040-1951(93)90118-4.
- Poliakov, A. N. B., Y. Y. Podladchikov, E. C. Dawson, and C. J. Talbot, 1996, Salt diapirism with simultaneous brittle faulting and viscous flow: Geological Society (London) Special Publication 100, p. 291–302.
- Ratcliff, D. W., S. H. Gray, and N. D. Whitmore, 1992, Seismic imaging of salt structures in the Gulf of Mexico: The Leading Edge, v. 11, p. 15–31, doi:10.1190/1.436876.
- Rohleder, S. A., W. W. Sanders, R. N. Williamson, G. L. Faul, and L. B. Dooley, 2003, Challenges of drilling an ultra-deep well in deep water—Spa prospect: Society of

- Petroleum Engineers/International Association of Drilling Contractors Drilling Conference, Amsterdam, Netherlands, February 19–21, 2003, SPE Paper 79810, 15 p.
- Roylance, D., 1996, Mechanics of materials: Hoboken, New Jersey, John Wiley & Sons Inc., 315 p.
- Rubey, W. W., and M. K. Hubbert, 1959, Role of fluid pressure in mechanics of overthrust faulting: 2. Overthrust belt in geosynclinal area of western Wyoming in light of fluid-pressure hypothesis: Geological Society of America Bulletin, v. 70, p. 167–206, doi:[10.1130/0016-7606\(1959\)70\[167:ROFPIM\]2.0.CO;2](https://doi.org/10.1130/0016-7606(1959)70[167:ROFPIM]2.0.CO;2).
- Sanz, P. F., and G. R. Dasari, 2010, Controls on in-situ stresses around salt bodies: 44th U.S. Rock Mechanics Symposium and 5th U.S.-Canada Rock Mechanics Symposium, Salt Lake City, Utah, June 27–30, 2010, American Rock Mechanics Association Paper 10-169, 12 p.
- Schultz-Ela, D. D., 2003, Origin of drag folds bordering salt diapirs: AAPG Bulletin, v. 87, p. 757–780, doi:[10.1306/12200201093](https://doi.org/10.1306/12200201093).
- Schultz-Ela, D. D., and M. P. A. Jackson, 1996, Relation of subsalt structures to suprasalt structures during extension: AAPG Bulletin, v. 80, p. 1896–1924.
- Schultz-Ela, D. D., and P. Walsh, 2002, Modeling of grabens extending above evaporites in Canyonlands National Park, Utah: Journal of Structural Geology, v. 24, p. 247–275, doi:[10.1016/S0191-8141\(01\)00066-9](https://doi.org/10.1016/S0191-8141(01)00066-9).
- Schultz-Ela, D. D., M. P. A. Jackson, and B. C. Vendeville, 1993, Mechanics of active salt diapirism: Tectonophysics, v. 228, p. 275–312, doi:[10.1016/0040-1951\(93\)90345-K](https://doi.org/10.1016/0040-1951(93)90345-K).
- Simulia, 2009, Abaqus user's manual, version 6.9: Providence, Rhode Island, Dassault Systèmes Simulia, <http://abaqusdoc.ucalgary.ca/v6.9> (accessed July 2011).
- Stefanescu, M., O. Dicea, and G. Tari, 2000, Influence of extension and compression on salt diapirism in its type area, East Carpathians Bend area, Romania: Geological Society (London) Special Publication 174, p. 131–147.
- Sweatman, R., R. Faul, and C. Ballew, 1999, New solutions for subsalt-well lost circulation and optimized primary cementing: Society of Petroleum Engineers Annual Technical Conference and Exhibition, Houston, Texas, October 3–6, 1999, SPE Paper 56499, 11 p.
- Terzaghi, K., 1925, Erdbaumechanik auf bodenphysikalischer Grundlage: Vienna, Austria, Leipzig u. Wien, F. Deuticke, 399 p.
- Timoshenko, S. P., and J. N. Goodier, 1970, Theory of elasticity: New York, McGraw-Hill, 567 p.
- Whitson, C. D., and M. K. McFadyen, 2001, Lessons learned in the planning and drilling of deep, subsalt wells in the deep-water Gulf of Mexico: Society of Petroleum Engineers Annual Technical Conference and Exhibition, New Orleans, Louisiana, September 30–October 3, 2001, SPE Paper 71363, 9 p.
- Willson, S. M., and J. T. Fredrich, 2005, Geomechanics considerations for through- and near-salt well design: Society of Petroleum Engineers Annual Technical Conference and Exhibition, Dallas, Texas, October 9–12, 2005, SPE Paper 95621, 17 p.
- Willson, S. M., S. Edwards, P. D. Heppard, X. Li, G. Coltrin, D. K. Chester, H. L. Harrison, and B. W. Cocales, 2003, Wellbore stability challenges in the deep water, Gulf of Mexico: Case history examples from the pompano field: Society of Petroleum Engineers Annual Technical Conference and Exhibition, Denver, Colorado, October 5–8, 2003, SPE Paper 84266, 10 p.
- Wood, D. M., 1990, Soil behavior and critical state soil mechanics: Cambridge, Cambridge University Press, 462 p.
- Zoback, M. D., 2007, Reservoir geomechanics: Cambridge, Cambridge University Press, 449 p.